The Electromagnetic Calorimeter of the GlueX Particle Detector

A Thesis
Submitted to the Faculty of Graduate Studies and Research
In Partial Fulfillment of the Requirements
for the Degree of
Master of Science
In
Physics
University of Regina

by
Stamatios Katsaganis
Regina, Saskatchewan
March, 2011

Abstract

This thesis focuses on the GlueX Barrel Calorimeter (BCAL), a key subsystem of the GlueX experiment, which is currently under construction. GlueX will shed light on an as yet unexplored area of the interaction between the fundamental constituents of matter, that of confinement. To achieve its goals, GlueX requires a hermetic detector with good acceptance and good energy and position resolution. To that end, a lot of effort has been spent on R&D in order to optimize the performance of the BCAL. Specifically, the effect of the thickness of the lead sheets, used to build the BCAL, on the performance of the BCAL was simulated using Monte Carlo techniques. Using the GEANT simulation package, three different geometry configurations were simulated and the shape of the longitudinal shower profile, energy resolution and the fractional energy deposition and energy leakage were extracted and the results comprise the first half of this thesis.

The second half of the thesis consists of an analysis of data collected in 2006 from a beam test performed at Jefferson Lab on a BCAL prototype module. The analysis was done in order to extract the energy resolution for several different angles of incidence, including the 90° which was used as reference.

Aknowledgments

I would like to thank my supervisor Dr. Zisis Papandreou and co-supervisor Dr. George J. Lolos, for the financial support that they provided throughout the duration of my studies and the completion of this work.

Dr. Andrei Semenov and Dr. Irina Semenova for their help when nothing made sense, they knew how to put it in order.

Last but not least, Dr. Christine Kourkoumelis for her support on both scientific and personal levels in the form of advice and guidance.

Dedication

To my parents, Christos and Ioanna.

Contents

List of Figures

List of Tables

Nomenclature

BCAL Barrel calorimeter

GUT Grand unified theory

LHC Large hadron collider

MPPC Multi pixel photon counter

PMT Photo-multiplier tube

PWA Partial wave analysis

QCD Quantum chromodynamics

QED Quantum electrodynamics

R&D Research and development

SAP Subatomic physics

SiPM Silicon photomultiplier

Chapter 1

Introduction

Subatomic physics (SAP) is the branch of physics encountered at very small scale systems. New accelerators and detectors, larger and more technologically advanced than their predecessors, have established SAP as the pinnacle of the technological advance, in the last 50 years. Applications ranging from military equipment to health instruments, and even to every day equipment or devices, utilize technology acquired from studying matter at the microscopic level. Nuclear power plants, smoke detectors and MRI scanners are only a few examples of the highly advanced applications of the knowledge gained from SAP experiments and theory.

In the last five decades, accelerators and detectors have boosted the energy scale up by at least three orders of magnitude (1 GeV to 1 TeV)[1] making modern experiments capable of 10^{-18} m resolution. This evolution affords physicists the capability to investigate matter interaction at the fundamental level, to ultimately unravel the laws that govern the universe and also answer the question of it's creation.

The Thomas Jefferson National Accelerator facility in Virginia U.S. is a facility

[1]Actually the Large Hadron Collider (LHC) is currently making this four orders of magnitude (14 TeV).

where physics experiments have been carried out for two decades. After more than a hundred and fifty completed experiments, the laboratory is under major upgrading in order to modernize the equipment and provide experiments with the latest state of the art tools. One of these experiments is GlueX, which will be hosted in a new experimental hall (Hall D) and is currently under construction. GlueX is planned by an international collaboration of 15 universities and more than 60 researchers.

1.1 Outline of thesis

A brief introduction to Quantum Chromodynamics (QCD) will be given in Chapter 2, starting with its history and ending with its salient features concerning the GlueX experiment. The motivation behind the realisation of GlueX experiment will also be discussed.

The GlueX experiment is currently (2010) under construction. The R&D phase for most of the subsystems comprising the detector, that will be used in Hall D, has been completed. The construction of the various components of the detector has been assigned to the collaborating institutions and is currently under way. Once completed, all components will be shipped to Jefferson Lab and the detector will be assembled. A team of researchers at the University of Regina, Saskatchewan, Canada, has been assigned the R&D as well as the construction of the Barrel Calorimeter (BCAL), a key component of GlueX. Chapter 3 holds the description of Hall D, the GlueX detector in general and the BCAL in more detail.

The topic of this thesis is the BCAL and is divided in two different subjects. Results from a series of Monte Carlo simulations, aimed at the performance optimization of the BCAL will be shown, in Chapter 4.

The second part of the thesis deals with analysis of test beam data collected in

2006 and is the topic of Chapter 5. In that chapter, energy resolution results will be shown from a beam test carried out in 2006 at Jefferson Lab.

Conclusions and further plans will be presented in Chapter 6.

Chapter 2

Introduction to QCD

2.1 High energy flash back

In the early 20^{th} century it was believed that all matter was comprised of "elementary" particles such as the proton, the neutron, the electron and the neutrino, in addition to the quantum of the electromagnetic field, the photon. The universe as we know it seemed to be made only from those particles. Around that time, the effort spent to understand the properties of the nuclear force, which is responsible for the binding of protons and neutrons (collectively called nucleons) forming the core (nucleus) of an atom, coupled with the discoveries regarding unstable particles in cosmic radiation, lead to advances in accelerators and detectors. The newer, larger and improved devices, in turn, lead to the discovery of a vast number of particles, many in short-lived unstable states, that were termed "hadrons" (strongly interacting particles).

This wealth of discoveries lead to a different picture:

1. The fundamental building blocks of matter are fermions, called quarks, with spin $\frac{\hbar}{2}$ and fractional electric charge such as ($+\frac{2}{3}$ e and $-\frac{1}{3}$ e), and the leptons,

like the electron and the neutrino, which have integer electric charge. The proton and the neutron then, are not fundamental particles since each is composed of three quarks.

2. These building blocks can interact with each other by exchanging "bosons" (particles with integer spin) that are the carriers of the four types of fundamental interactions or fields: gravity, electromagnetic, weak and strong forces. At the mass and distance scale of particle physics, gravity is less significant than the other three and therefore its contribution is neglected.

   - The electromagnetic force is responsible for most of the processes occurring outside the atomic nucleus, together with the binding of atoms and molecules, and is very accurately described by Quantum Electrodynamics (QED).
   - The weak interaction is responsible for the beta decay of unstable nuclei and has been unified with the electromagnetic force under the electroweak force described by the Electroweak Theory.
   - The strong force is responsible for the confinement of the quarks inside the nucleons and also for the binding of the nucleons to form a nucleus, described by Quantum Chromodynamics (QCD).

   Both the weak and the strong forces have very small range (at the order of magnitude of 1 fm[1])

Although simple at first glance, this picture has some peculiarities. The fractionally charged quarks have never been observed as free particles; they are always bound into hadrons. Quarks appear in a variety of types or "*flavours*" (six are known), just

[1] fm is a unit of length and stands for femtometer, 1 fm = 10^{-15} m

like the leptons which come in three charged types and three neutral types. The

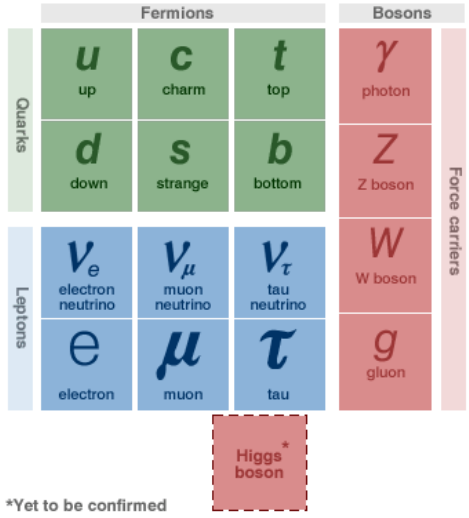

Figure 2.1: The Standard Model is a theory about the way elementary particles interact with each other. It has 16 particles, 12 of them are matter particles (fermions) and the other four are the interaction carriers (bosons). The Higgs boson is there to explain how these particles acquire their mass. The direct experimental proof of the existence of the Higgs boson is yet to be observed.

mechanism that keeps the quarks trapped in hadrons, as well as the existence of six quarks, when in fact it seems that all the matter in the universe is comprised by only two types of quarks, one charged lepton and one neutral lepton, is not yet been fully understood.

In an effort to come up with one theory that would include all four fundamental interactions, in a sense that these are just the different manifestations of the "*one*" interaction (often referred to as Grand Unified Theory (GUT)), the weak and the electromagnetic force were successfully unified into the electro-weak interaction. The coupling between the fermion matter and the boson is the same in both and the only difference is their range. The carrier of the electromagnetic force, the photon, which has zero mass, has infinite range as opposed to the massive carriers of the weak force

($W^{\pm}$, Z^0)[2], which have very short range (on the order of the nucleus diameter). At high energy, a lot higher then the mass of the $W^{\pm}$, Z^0 bosons, the electromagnetic and the weak nuclear forces have the same strength.

The reason that the symmetry between the forces is violated at lower energies and the bosons have differing masses is also not yet resolved. However, it is understood that the intensity of each interaction (their coupling constants) is not fixed and depends on the energy scale. As the energy increases the strong force becomes weaker and it is expected that there is an energy scale where the electro-weak interaction and the strong interaction unify.

According to the most widely known theory about the creation of our universe, it is believed that everything is the result of a "*Big Bang*", a violent expansion of an energy "*bubble*", from which all the particles, quarks, leptons and quanta, were created. At the very first moments of the creation of the universe, the energy density was so high that all interactions were unified. The result of the "*Big Bang*" is the ever expanding and cooling down universe. Therefore, high energy physics research is a time travel back to the initial conditions of the universe which defined it as it is known today [1].

2.2 Gluons

Quantum Chromodynamics is a quantum field theory of the strong force that explains the interaction between particles with colour charge, such as quarks and gluons. In Quantum Chromodynamics, particles interact through the strong force by exchanging gluons, which are the carriers of the strong force (much as photons are the carriers of the electromagnetic force in Quantum Electrodynamics).

[2] $W^{\pm}$, Z^0 have been found to have roughly the mass of a hundred protons.

Colour describes an additional degree of freedom that can take on six values. Every quark carries one of the colours red, green or blue and every antiquark carries the respective anticolour. This is quite the variety compared to the electric charge that can only take two values: plus (+) and minus (-). In addition, gluons also carry colour, unlike the photon which does not possess electric charge, therefore gluons interact with quarks *and* with each other.

2.3 Quarks and Hadrons

All matter consists of quarks and leptons, which are considered to be fundamental particles and therefore have no structure: their size is less than 10^{-17} m. Quarks have fractional electric charge and come in six flavours u (*up*), d (*down*), s (*strange*), c (*charm*), t (*top*), b (*bottom*) (Figure 2.1). The u and d quarks are the lightest of the six and have almost the same mass[3]. Antiquarks have the same mass and behaviour under strong interactions as the corresponding quarks but opposite charge.

The mass of the quarks is a rather arbitrary quantity, since they have not been observed free: they are confined in hadrons. Hadrons are strongly interacting particles made of two types of quark combinations:

- Baryons which consist of three quarks (qqq)
- Mesons consisting of quark-antiquark combinations ($q\bar{q}$)

Since quarks have half-integer spin, the baryons have half-integer spin (fermions) and the mesons have integer spin (bosons) [2]. This description is termed the Simple Quark Model and does not involve explicit gluonic degrees of freedom, which must exist according to QCD.

[3]The difference in the mass of the *up* and *down* quark is approximately 1 MeV.

2.4 Mesons

Mesons consist of a $q\bar{q}$ pair bound together by the strong force. Starting back in the 1960's, a plethora of mesons have been discovered in particle physics experiments. Each meson is classified according to its quantum numbers, which are represented by a J^{PC} combination, where $\vec{J}$ is the total angular momentum, P is the parity and C is the charge conjugation. The total angular momentum is the vectorial sum of the orbital angular momentum quantum number denoted by $\vec{L}$ and the total spin ($\vec{S}$), $\vec{J} = \vec{L} + \vec{S}$. Parity ($P$) expresses the symmetry of the meson under spatial transformations and charge conjugation expresses the symmetry under the exchange of the electric charge. Both P and C are assigned the plus (+) value if the meson's wavefunction is symmetric or the minus (-) if it is antisymmetric under the corresponding transformation. Expressed in mathematical form these rules read $P = (-1)^{L+1}$ and $C = (-1)^{L+S}$.

The orbital angular momentum L can take values in the set $\{L = 0, 1, 2, \dots\}$. The spin S of the system is given by the vectorial sum of the spin of the two fermions and therefore can be either $S = 0$ when the fermions have anti-parallel spins ($\uparrow\downarrow$) or $S = 1$ when the fermions have parallel spins ($\uparrow\uparrow$) ($S = 0, 1$). Under the constraints set by the symmetry and the possible values of L and S, not all combinations of J^{PC} are allowed. For example if $L = 0, 1$ then the set of allowed J^{PC} reads $\{0^{-+}, 0^{++}, 1^{--}, 1^{+-}, 1^{++}, 2^{++}\}$. J^{PC} combinations such as $\{0^{+-}, 1^{-+}, 2^{+-}\}$ violate at least one of the rules of the Simple Quark Model.

Using the lightest three quarks (u, d, s), for each J^{PC}, there can be nine different mesons. In other words, for any given J^{PC} combination there is a family of nine mesons, called nonets. This is a convenient and elegant way to classify them, but also a way to predict the existence of mesons that have not been discovered yet. A

nonet, corresponding to $J^{PC} = 0^{-+}$, is shown in Figure 2.2.

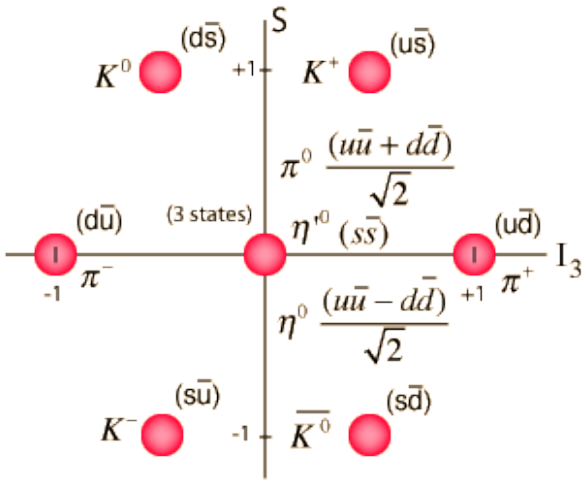

Figure 2.2: Schematic diagram of the nonet of mesons corresponding to $J^{PC} = 0^{-+}$. The quark flavour combination for each meson can also be seen.

2.5 Glueballs

QCD predicts the existence of hadrons consisting only of gluons (gg, ggg), called *glueballs*, based on the self interacting nature of the gluons. Experiments that attempted to identify *glueballs*, like the Crystal Barrel experiment [3,4], failed to do so because of ambiguous evidence. This ambiguity is due to a phenomenon called *mixing*. Mixing is a result of the internal workings of the quantum theory. Any quantum state defined by a set of quantum numbers is a superposition of all the mass eigenstates (observable particles) that have the same quantum numbers. That said, a measurement, which results in the identification of the quantum numbers defining the state of a particle, is subject to the uncertainty arising from mixing. *Glueballs* lying in the low mass region ($< 4 - 5\,GeV/c^2$) are expected to have the same quantum numbers

as other hadrons and, due to mixing, their identification can be hard to accomplish. However, a series of experiments have shown excess states and this is an indication that glueball states are among them.

2.6 Hybrid Mesons

There exists another combination involving quarks and gluons that is predicted by QCD and Lattice QCD[4] [5]: *hybrids*. Hybrids are hadrons too and the simplest formation is that of a meson consisting of a $q\bar{q}$ with a valence gluon, called a *hybrid meson ($q\bar{q}g$)*. Some of the models attempting to describe hybrid mesons are *The Bag Model*, *The Flux Tube Model* and the *Constituent Quark Model* [6–10].

Figure 2.3: The colour field between a $q\bar{q}$ pair (meson) according to the flux tube model. The interaction between the gluons, due to their colour charge, increases the density of the dynamic lines between the $q\bar{q}$ pair, creating a tube-like area of colour flux.

According to the *Flux Tube Model*, the colour-field dynamic lines between a $q\bar{q}$ pair, due to the attractive interaction between gluons, form a tube [11, 12]. A schematic representation of the colour-field lines is shown in Figure 2.3. *Hybrid mesons* can also be thought of as an excited state of the gluonic field binding the $q\bar{q}$ pair. The description of this state in quantum theory requires the addition of a new

[4]Lattice QCD is QCD formulated on a discrete Euclidean space time grid. Since no new parameters or field variables are introduced in this discretization, Lattice QCD retains the fundamental character of QCD. Lattice QCD provides a non-perturbative tool for calculating the hadronic spectrum and the matrix elements of any operator within these hadronic states from first principles.

quantum number represented by the gluonic angular momentum ($\vec{m}$). This added quantum number has to be accounted for when the J^{PC} combinations are calculated and doing so leads to J^{PC} combinations that were forbidden by the Simple Quark Model, which now corresponds to a ground state flux tube ($\vec{m} = 0$) binding the $q\bar{q}$ pair. Therefore, there exist nonets that have *"exotic"* J^{PC} combinations, in addition to the conventional ones. The existence of these previously forbidden nonets is a consequence of the *hybrid* nature of the mesons and the mesons carrying these quantum numbers are called *exotic hybrid mesons*.

Identifying *hybrid* mesons presents an advantage compared to *glueball* searches. The exotic members of the *hybrid* meson family have unique quantum numbers and cannot mix with ordinary quarkonia ($q\bar{q}$). This is fascinating because detecting exotic mesons is definitive proof that hybrid mesons exist, which in turn validates QCD in the confinement region and the *Flux Tube Model*.

The mapping of exotic hybrid mesons will shed light on the confinement of the fundamental building blocks of matter and represents a very significant piece of new knowledge. The GlueX experiment will attempt to provide the scientific community with this knowledge by mapping the *exotic hybrid meson* spectrum [13].

Chapter 3

The GlueX detector

3.1 Overview

The ultimate goal of the GlueX experiment is the mapping of gluonic excitations in the form of hybrid mesons with masses up to 3 GeV/c^2. To achieve this, the identification of these excited states, by determining their J^{PC} quantum numbers and their decay modes, is crucial. This is accomplished by partial wave analysis (PWA), which depends greatly on how well the kinematic attributes of exclusive reactions can be resolved. This means that the GlueX detector must be capable of detecting the products of the excited meson decays and measuring their properties with good resolution and full acceptance.

The energy of the incident photon beam must be well chosen in order to address the following two requirements:

- Adequate energy is needed for the production of the required masses (m_X) with sufficient cross section and sufficient forward boost so that their decay products can be detected with sufficient resolution. Production of hybrids with masses up to 2.5 GeV/c^2 will require an incident photon beam of at least 9 GeV as

shown in Figure 3.1.

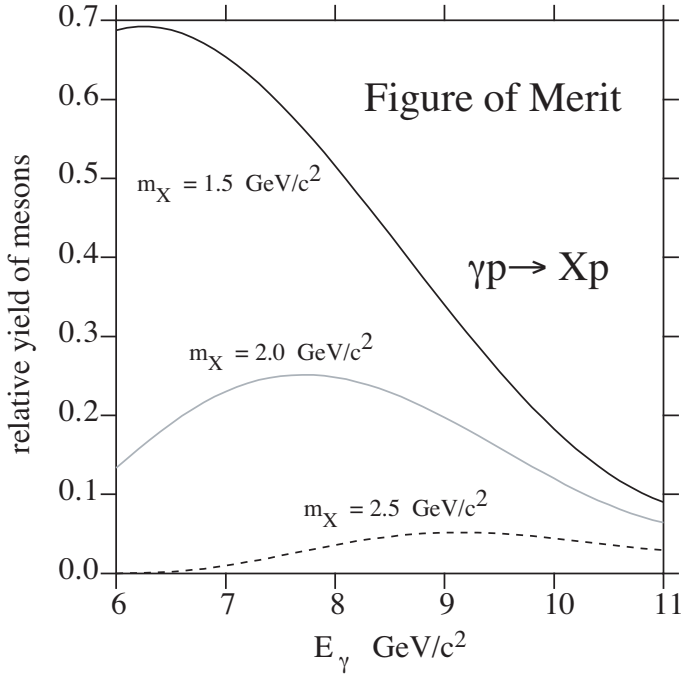

Figure 3.1: The relative yield of exotic mesons plotted versus the energy of the incident photon beam. Generation of an adequate number of mesons at the mass scale of 2.5 GeV/c^2 will require approximately 9 GeV photon beam.

- Linear polarization and sufficient beam flux are crucial elements for PWA and both properties depend on the energy of the beam. This is related to the fact that states of linear polarization, in contrast to states of circular polarization, are eigenstates of reflectivity. The linearly polarized photon beam will be produced by coherent bremsstrahlung[1]: a diamond wafer ($\sim 15\mu m$ thin) will be used as a target for the 12 GeV electron beam. Especially selected orientations of the diamond crystal lattice with respect to the electron beam can force the atoms of the diamond wafer to recoil together (coherently) resulting in enhanced emission of photons at particular energies and yielding linearly

[1]Bremsstrahlung is the phenomenon where a charged particle emits photons while decelerated by interacting with the electromagnetic field of a nucleus.

polarized photons. The beam energy cannot be too high because the degree of linear polarization and photon flux at the coherent peak drop as shown in Figure 3.2.

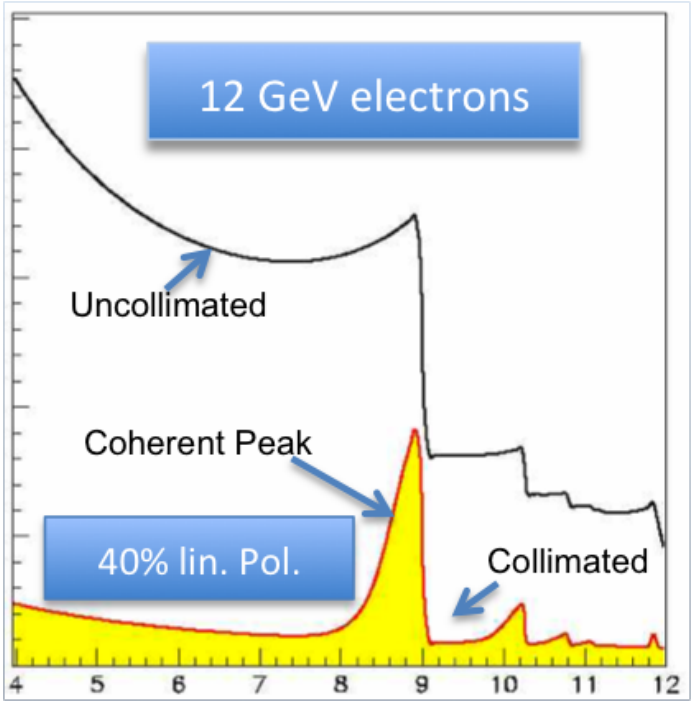

Figure 3.2: The spectrum of the coherent bremsstrahlung photon beam as a function of beam energy (horizontal axis). 40% of the beam consists of linearly polarized photons. The flux of the collimated beam (plotted on the vertical axis) peaks at approximately 9 GeV. To maintain flux and degree of linear polarization adequately high for the PWA analysis, the energy of the photon beam must be kept at the region of the peak.

Driven by these requirements, the GlueX detector must be a hermetic detector with nearly 4π coverage, good energy and timing resolutions and also optimized for the required energy range of the photon beam [14].

3.2 General description

The GlueX detector is cylindrically symmetric around the beam line and employs a superconducting solenoid yielding a 2.25 Tesla magnetic field as shown in Figure 3.3. The magnetic field is capable of trapping most of the low energy electrons generated in the target[2] in a tight cone around the incident photon beam and thus keeping them from overwhelming the detectors, particularly the tracking devices surrounding the target and downstream of it.

The photon beam (delivered by the accelerator in Hall D) will be incident on a 30 cm long liquid hydrogen target. The target is surrounded by the start counter, which contributes the trigger for charged events. Outside the start counter is the central drift chamber (CDC), responsible for the detection of charged particles, having polar emission angles greater than 16°. For those with polar angles less than 16°, the forward drift chamber (FDC) will be used. Actually, the FDC can detect particles with angles less than 25°, therefore there is a region (16° to 25°) where the two subsystems are combined in detection of particles.

Outside the CDC is the barrel calorimeter (BCAL), capable of detecting both neutral and charged particles. Downstream is the time-of-flight wall (TOF), made of plastic scintillator bars, and the forward calorimeter (FCAL) made of lead glass blocks that will detect photons in the region up to 16°. Space between the cylindrical detectors and the TOF has been reserved for an –as yet– unspecified particle identification unit (PID). The resulting design is a nearly 4π (hermetic) detector as required by the GlueX experiment.

[2]Low energy e^+, e^- generated by atomic processes (small angle scattering) will spiral down the beam direction.

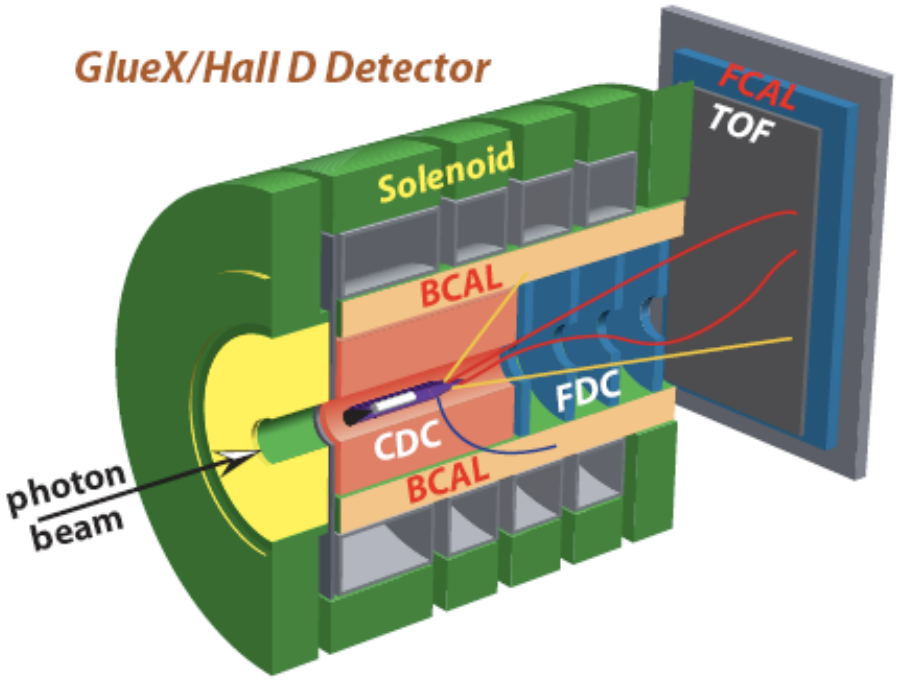

Figure 3.3: Overview of the GlueX detector. From the inside to the outside, the start counter will provide triggering (firing) information, while the CDC will detect charged particles. The BCAL is optimized for neutrals but can also detect charged particles. Neutral and charged particles traveling towards the forward region, at polar angles less than 16°, will be detected by the FDC, the FCAL and the TOF. The superconducting solenoid will provide the necessary magnetic field for momentum definition of charged particles.

3.3 Introduction to electromagnetic calorimetry

3.3.1 Energy deposition mechanisms

Before a detailed description of the BCAL is presented, it is appropriate to look at the physics processes on which the detection of particles of the BCAL is based. A photon (γ) is affected by four physical processes:

- Electron-positron pair production. This process occurs when a photon with energy higher than twice the rest mass of an electron[3] creates an electron-positron pair, in the presence of an atom ($\gamma \rightarrow e^- + e^+$). The electromagnetic field needed for pair production is provided mostly by the absorber' s nuclei, but atomic electron field can also contribute. When a relatively high-energy electron is incident on a dense absorber, another process that is crucial to the energy deposition distribution takes place: bremsstrahlung. Bremsstrahlung occurs when high energy electrons or positrons interact with the Coulomb field of the nuclear field and results in the emission of large numbers of photons. The sequence of pair production and bremsstrahlung continues for as long as the generated particles have sufficient energy. It is obvious that through this repeated process a multiplication of shower particles occurs. The result is an *electromagnetic shower* consisting of thousands of particles: photons, electrons and positrons. Pair production is the dominant process at high energies.

- Incoherent scattering (Compton). Compton scattering occurs when a photon is scattered by an atomic electron and the transfer of momentum and energy are sufficient to set the electron in an unbound state. It is very likely to happen at low to medium energies (0.5 MeV to 10 MeV). In fact half of the

[3]Mass of the electron in its own reference frame.

energy deposition occurs due to the Compton scattering when the energy of the secondary gamma rays created by other processes becomes sufficiently low.

- The photoelectric effect. This process is most likely to occur at low energies (less than 0.5 MeV). A photon is absorbed by an atom and is left at an excited state. The excited atom returns to its ground state by emitting electrons (beta radiation) or X-rays (gamma radiation). The photoelectric cross section depends on the Z value of the absorbing material.

- Coherent scattering (Rayleigh). This is also likely to happen at low energies. The photon is deflected by the atomic electrons without losing energy. Rayleigh scattering does not contribute to the energy deposited in the absorber but affects the spatial distribution of the energy deposition.

When the energy of the shower particles decreases, they deposit their energy in the absorber by ionization as mentioned earlier in this section. The electrons eventually get absorbed by an ion and the positron annihilates with an electron and produces two photons. The energy deposited in the first layers of the absorber increases due to the multiplication of the shower particles. However, as the shower develops the average energy of the generated particles decreases and multiplication is halted. The depth in the absorber where the multiplication stops is referred to as the *"shower maximum"*. Beyond the *"shower maximum"* the number of shower particles decreases and so does the energy deposition [15].

3.3.2 Calorimeter response

Based on the way the signal is extracted, calorimeters are categorized in two groups:

- Homogeneous calorimeters, where the entire calorimeter volume is sensitive to the particles and contributes to the generated signals, like the FCAL.

- Sampling calorimeters, in which the absorption of the particles and the generation of signals is assigned to different materials. The absorbing material referred to as *"passive medium"* is a high density material in which the shower develops. The sensitive material referred to as *"active medium"* is where light or charge signal is generated. BCAL is an example of such a calorimeter.

The signal from an electron or photon absorbed in a sampling calorimeter is a contribution of the ionization or excitation of the *active medium* by all electrons and positrons of the shower that traverse its volume [15].

A detailed description of the electromagnetic sampling calorimeter is presented in the next section.

3.4 The GlueX electromagnetic barrel calorimeter (BCAL)

The BCAL will be 390 cm long and will be placed immediately inside the solenoid magnet, which limits its outer radius to $\sim 90\ cm$. The inner radius is based mainly on the volume required for particle tracking and is set at $\sim 65\ cm$ (making the thickness of the BCAL approximately $\sim 25\ cm$), as shown in Figure 3.4a and also tabulated in Table 3.1.

The BCAL is divided into 48 equally-sized modules Figure 3.4c. Each module has a trapezoidal cross section as shown in Figure 3.4d. The internal structure of these modules is based on the design of the EmCal calorimeter build by the KLOE collaboration for the KLOE experiment at $DA\Phi NE$-Frascati [16–18]. KLOE and

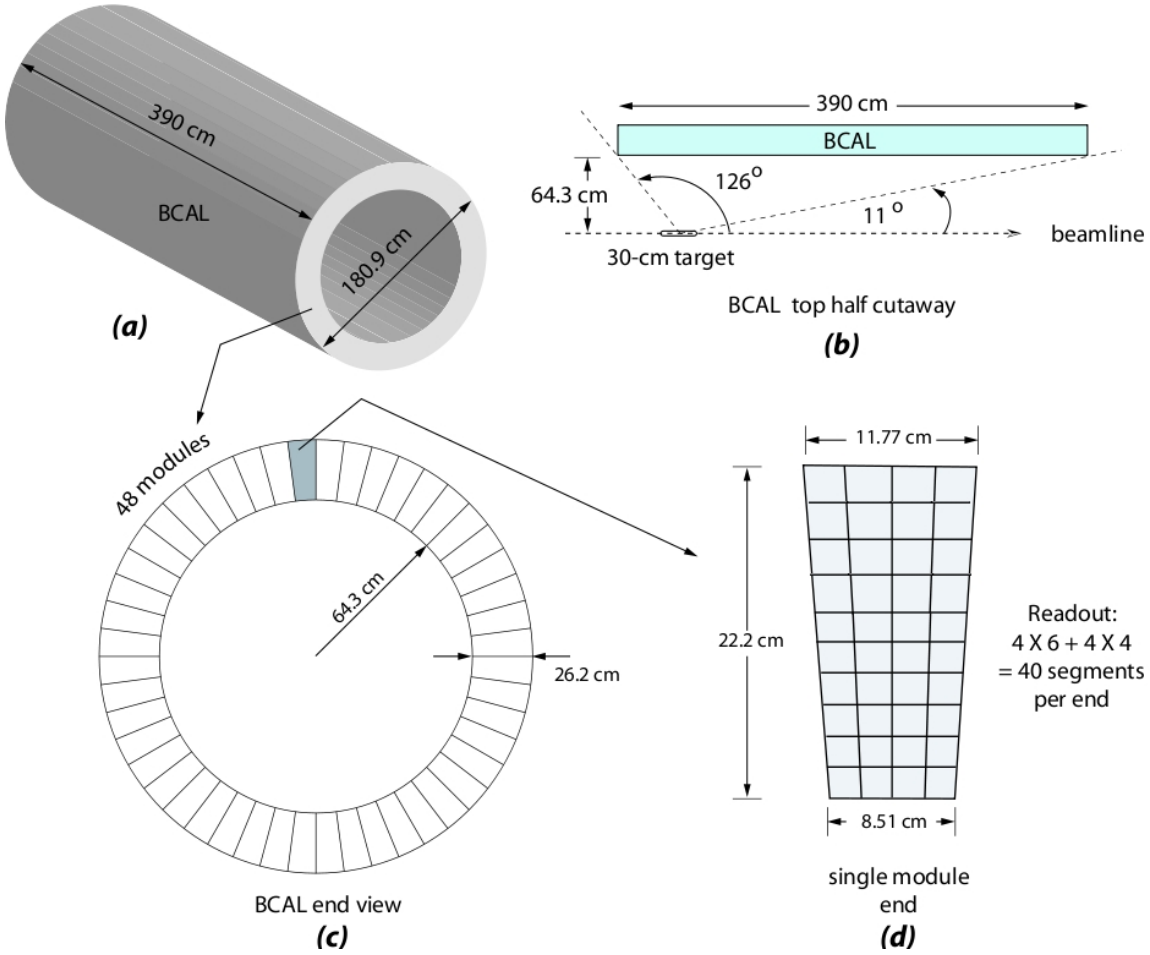

Figure 3.4: General geometrical attributes of the barrel calorimeter and its modules.

GlueX calorimeters both employ lead/scintillating fibre (Pb/SciFi) matrix with photo-sensors at either end for energy and timing measurements.

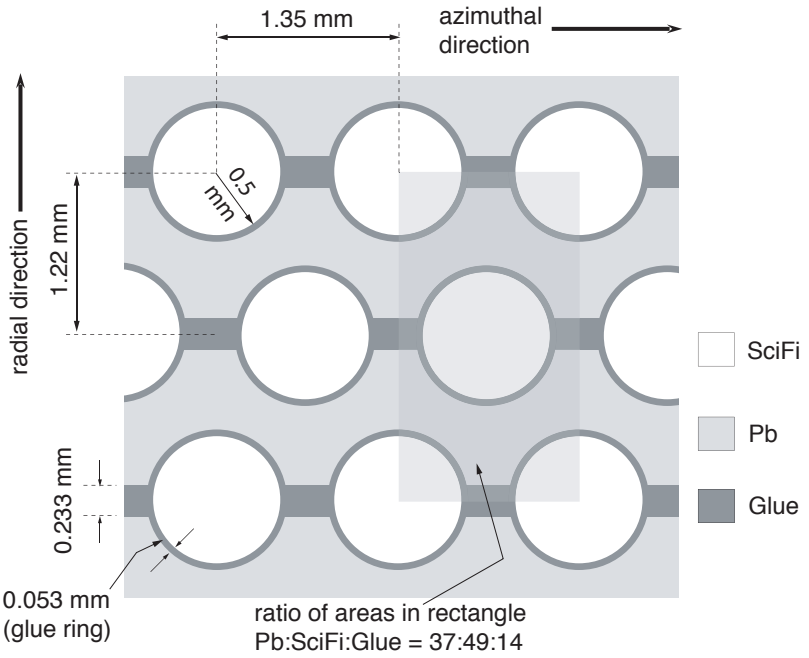

Figure 3.5: Cross section of the lead/scintillating fibre matrix. The distance between fibres is 1.35 mm in the azimuthal direction and 1.22 mm in the radial direction. The resulting lead to scintillating fibre to glue volume ratio of 37:49:14.

The Pb/SciFi matrix is made of thin (0.5 mm) lead sheets with embedded layers of scintillating fibres of 1 mm diameter and glued together with Bicron-600[4] optical epoxy as shown in Figure 3.5. A brief description of the process is provided here. The lead sheets (Figure 3.6a) are mechanically processed[5] and grooves for the fibres are created (Figure 3.6b) by rolling the sheets between two grooved steel cylinders. Then a layer of epoxy is applied on the lead sheet, the scintillating fibres are placed into the grooves and another sheet of lead is glued on top. After about 10-14 of those layers are stacked, the resulting matrix is pressed with a pneumatic press until the

[4]Saint-Gobain Crystals and Detectors, USA (`www.bicron.com`).

[5]The construction of the GlueX barrel calorimeter including the mechanical process is currently under way at the University of Regina.

epoxy cures. The process is repeated until the desired matrix height of 185 layers is reached. A cross section drawing of the resulting matrix can be seen in Figure 3.5 and a photograph in Figure 3.6d. The matrix has a lead to scintillating fibre to glue volume ratio of 37:49:14.

The scintillating fibres used for the GlueX BCAL are double-clad fibres with superior performance characteristics compared to those used by KLOE in that they capture up to 50% more light than the single-clad fibres in KLOE. More light at the end of the fiber means better resolution, particularly at the lower end of the spectrum of the detected photons. The attenuation length of the fibres used by GlueX is also longer, which means less light is absorbed over the entire energy spectrum.

The readout consists of 80 photo-sensors, 40 at either end. Each module is divided into two main regions, the inner and the outer part with respect to the radial direction. The inner part is divided into 24 readout cells in a 4×6 fashion while the outer region utilizes a coarser segmentation of 16 readout cells in a 4×4 fashion as shown in Figure 3.4 (d). The finer segmentation of the inner region is required for optimal energy and momentum resolution, since the highest energy deposition is expected in this region even for the most energetic particles. On the other hand, the outer region is expected to contain only a small fraction of the shower's energy, which justifies the reduced number of detection units. This configuration will be utilizing a total of 3840 photo-sensors, which represents a non-trivial challenge as far as positioning and mounting are concerned.

The intense magnetic field and gradients at the location of the BCAL's readout place stringent requirements on the selection of devices that can function efficiently in such an environment. Several technologies were considered before silicon photomultipliers (SiPMs) were chosen. They are based on rather recent developments

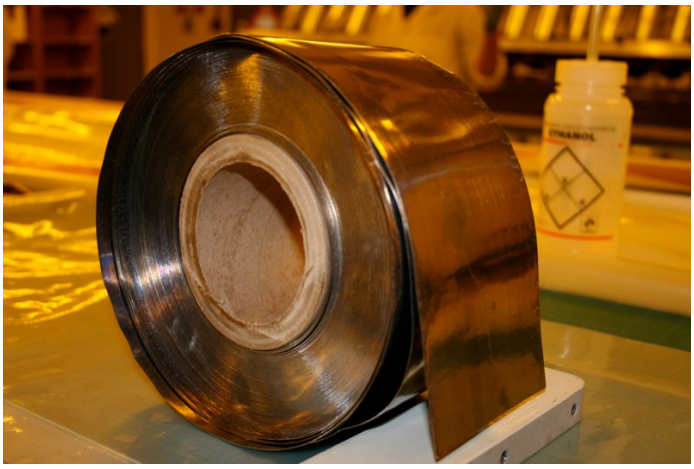

(a) A 0.5 mm thick lead sheet before the swaging process.

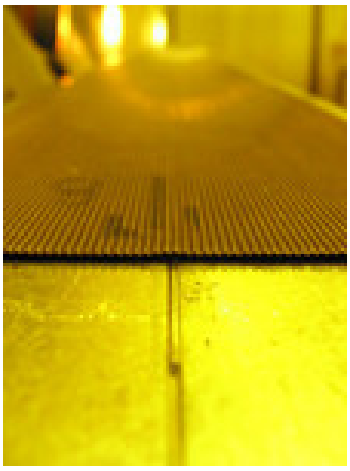

(b) The lead sheet after the swaging process showing the grooves where the scintillating fibres will be layed.

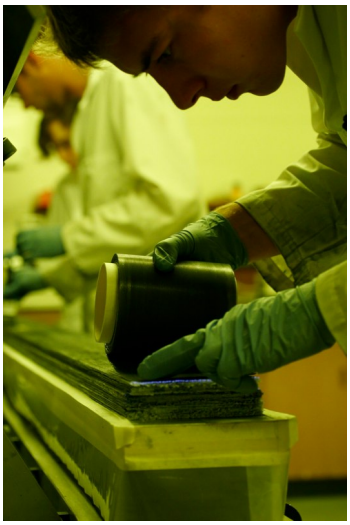

(c) Laying down another lead sheet.

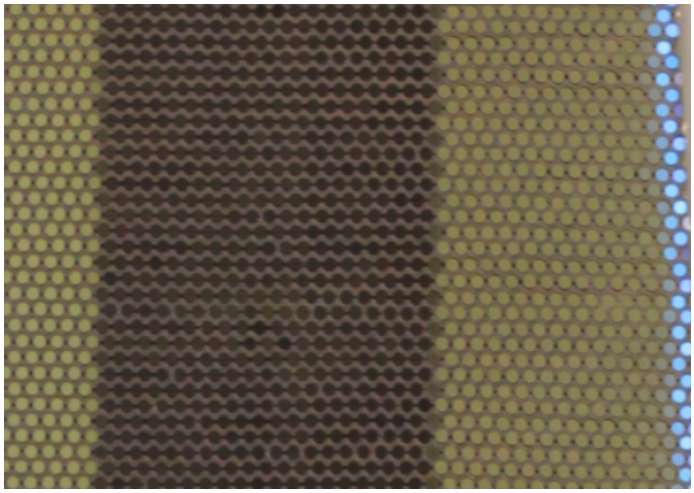

(d) Cross section photograph of the completed Pb/SciFi matrix. The darker region represents the shadow created by a straight edge ruler placed on the opposite end of the matrix and viewed through the calorimeter module.

Figure 3.6: Photos depicting the various stages of the BCAL construction.

Table 3.1: Main properties of the GlueX BCAL

Parameter	Size
Length	390 cm
Inner radius	65 cm
Outer radius	90 cm
Fibre diameter	1 mm
Lead sheet thickness	0.5 mm
Number of fibres	780,000
Number of readout cells	3840
Weight	25 metric tons

in semiconductors: they consist mainly of a p-n (or n-p) junction and operate in a limited Geiger avalanche mode, with each of their tiny $(20 - 50\ \mu m)$ pixels firing digitally (0 or 1) and the combination of 3000-5000 pixels in one macro cell leading to an analog signal proportional to the incident light. GlueX pushed industry[6] to assemble 16 such $3 \times 3\ mm^2$ macrocells into a 4×4 array functioning as a single unit with a sensitive area of 1.26 cm^2. SiPMs are immune to magnetic field and have a good photon detection efficiency (15-25%).

The coupling of the SiPM photo-detectors to the BCAL is another challenge that GlueX has to overcome. The effective detection area of a SiPM is significantly smaller than the area of any of the readout cells and therefore coupling of the SiPM to a light guide (collector) to the BCAL ends is required. Table 3.1 summarizes several construction related properties of the BCAL.

As mentioned earlier, the KLOE calorimeter serves as a model for the construction and also as a reference for the performance of the GlueX BCAL. The final energy and timing resolution for KLOE [16] were

$$\frac{\sigma_E}{E} = \frac{5.4\%}{\sqrt{E(GeV)}} \oplus 0.7\%$$

[6]The Hamamatsu S10943 MPPC was selected by the GlueX collaboration as the SiPM array for the production (final) phase of the BCAL.

and

$$\sigma_t = \frac{56\ ps}{\sqrt{E(GeV)}} \oplus 133\ ps$$

respectively. These numbers serve as benchmarks for the GlueX BCAL.

Chapter 4

Lead Thickness and BCAL Performance

4.1 Motivation

As explained in Chapter three, the photon detection efficiency of SiPMs is good ($\sim 15\%$ to $\sim 25\%$), however, they could clearly benefit by having more light incident upon them because both energy and timing resolution depend on the number of photoelectron statistics generated.

Light attenuation inside the fibres results in a reduction of the amount of light reaching the surface of the SiPM, particularly for particle impact points far from the sensor. For particles entering the BCAL with energies higher than 100 MeV, the light generated in the fibres is usually high enough to be detected by the photo detectors at either end of the module. Less energetic particles ($< 40\ MeV$) may not be detectable at one or both ends. Obviously, the more energy deposited in the scintillating fibres of the BCAL, the more accurately a particle's energy can be determined by the SiPM.

Increase of the light yield can be achieved by increasing the active volume (scintillating fibre) and decreasing the inert volume (lead). However, this results in a reduced electromagnetic density of the module in terms of radiation lengths[1](X_0) [19] and thus reduced capability to contain the energy of the resulting electromagnetic shower for energetic particles (>400 MeV) at normal incidence to the module. Indeed, for energetic particles a significant amount of energy leaks from the back of the calorimeter and thus degrades the energy resolution. This, however, is no concern for low energy particles, which deposit most of their energy in the first few centimeters of the inner segments of the module.

The motivation of this study is to test a mixed configuration of the geometry of the BCAL that would best address both desired goals. First, to capture as much energy of the higher energy particles and second, for low energy, particles to have the best possible ratio of energy deposited in the scintillating fibres over the amount of energy lost in the non-sensitive materials of the BCAL.

4.2 Description of setup

4.2.1 Geometrical configuration

Three geometrical configurations were simulated.

- 'Nominal' geometry with radial pitch of 1.24 mm.
- 'Thin' geometry with a resulting radial pitch of 1.11 mm.
- 'Hybrid' geometry is a mixture of nominal and thin geometry.

[1]Radiation length is the mean distance traveled by an electron or photon until it loses all but 1/e of it's energy, in the given material.

The nominal geometry mirrors what was achieved following the construction of the lead, scintillating fibre and glue matrix for the first full scale prototype (Prototype 1)[2]. The simulated thin geometry consisted of thinner lead sheets –than the nominal– resulting in a radial pitch of 1.11 mm. In the hybrid geometry, the first 6 cm (first 3 segments) were made of the thin 1.11 mm pitch geometry and the rest (6 cm to 22.5 cm) were made of the nominal geometry of 1.24 mm pitch. Additional simulations were carried out using other thicknesses but were not pertinent to this study and therefore not reported here.

Thinner lead sheets impact the detailed x-y geometry of the matrix. By using knowledge from the KLOE calorimeter prototypes [20], the following observations on the shape of the lead sheets can be drawn. When the sheets are thick enough, about 0.5 mm, the swaging process is very precise in formulating the grooves where each fibre will be glued. When the sheet thickness decreases there is not enough material for the grooves to be well formulated. Instead, the lead sheet assumes a wavy form, and most of the space between fibres is now filled by glue. These configurations are shown in Figures 4.1 and 4.2.

In all simulations, cladding has been included in the fibre volume description. This effectively reduces the fibre core diameter by 10%, as compared with past simulations [21] that assumed that the entire fibre diameter of 1 mm consisted of core material. The BCAL will employ double-clad fibres and it is more accurate to include this factor in the simulation.

[2]Prototype 1 was constructed in 2004 using blue-emitting Pol.Hi.Tech 0.44 fibres.

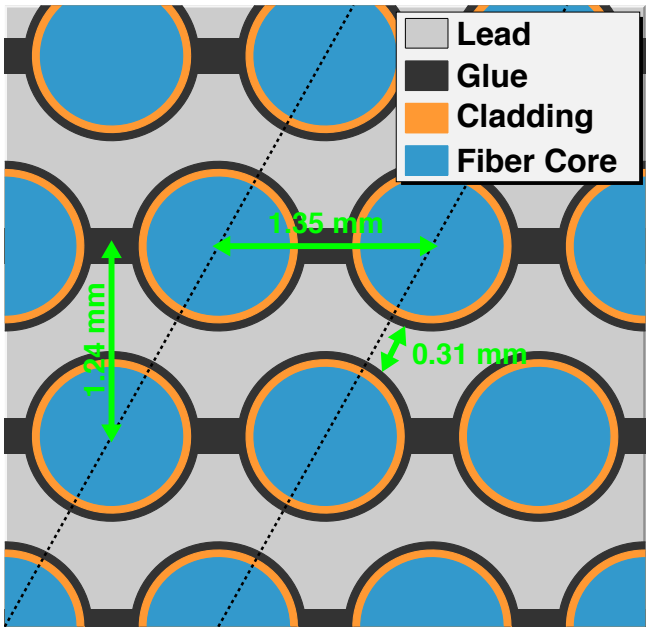

Figure 4.1: Nominal matrix geometry having a 1.24 mm radial pitch and a 0.31 mm lead thickness between diagonally displaced fibres, corresponding to a 0.5 mm sheet thickness.

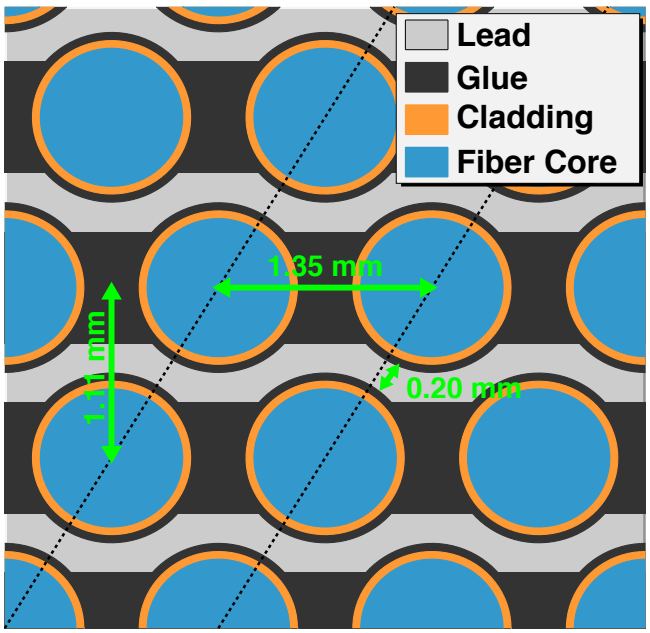

Figure 4.2: Thin matrix geometry having a 1.11 mm radial pitch and a 0.2 mm lead thickness between diagonally displaced fibres, corresponding to a 0.5 mm sheet thickness.

4.2.2 Radiation length (X_0) and Molière Radius (R_M)

Each module is a matrix that consists of three components: lead, fibre and epoxy. For the physics processes that affect the BCAL performance, the depth of the module in radiation length units is more relevant than its actual thickness in units of length. In addition, it is instructive to characterize the lateral development of the electromagnetic shower in terms of the Molière radius[3] [19]. The radiation length is given by

$$\frac{1}{X_0} = \sum_j \frac{w_j}{X_j} \tag{4.1}$$

where w_j is the fraction by weight of each component and X_j is the radiation length of the j^{th} component. The Molière Radius is given by

$$R_M = X_0 \frac{E_s}{E_c}, \;\; E_s \approx 21 \; MeV, \;\; E_c \text{ is the critical energy}^4 \tag{4.2}$$

There are several ways to calculate X_j for the three components of interest [22]. Table 4.1 summarizes all data for each component needed to calculate the radiation length (X_0) for each geometry used in the simulations. Table 4.2 summarizes the radiation length and Molière Radius results. As expected X_0, and R_M are larger in the thin geometry as a result of its reduced capacity in containing the electromagnetic shower.

[3]The radius of a cylinder whose axis of symmetry is parallel to the direction of the shower and contains 90% of the energy of the shower is defined as the the Molière Radius (R_M).

[4]More information about E_c is given on page 37.

Table 4.1: Information for the materials comprising the module. As SciFi and epoxy are made of more than one material, their effective A and Z are tabulated here.

Component	A	Z	ρ (g/cm^3)	X_j (cm)
Pb	207.2	82	11.35	0.56
SciFi	11.163	5.615	1.049	42.46
Glue	11.291	5.686	1.180	37.36

Table 4.2: X_0 and R_M as calculated for the nominal geometry of 1.24 mm radial pitch and the thin lead geometry of 1.11 mm radial pitch, respectively.

Geometry	Component	w_j	Z_{eff}	A_{eff}	X_0 (cm)	R_M
nominal	Pb	0.8719	72.22	182.10	1.40	3.54
	SciFi	0.0958				
	Glue	0.0323				
thin	Pb	0.7290	61.31	154.09	2.59	5.57
	SciFi	0.1691				
	Glue	0.1019				

Table 4.3: Depth of the module expressed in radiation length units. The hybrid module is constructed of a 1.11 mm pitch inner part of thickness 2.32 X_0 while the outer part has 1.24 mm pitch and is 12.18 X_0 thick.

Geometry	Front part (X_0)	Rear part (X_0)	No. of X_0
nominal	-	-	16.47
thin	-	-	8.90
hybrid	2.32	12.18	14.51

4.2.3 Simulation Code

A series of simulations have been carried out using GEANT3 [23]. All past BCAL simulations were based on the nominal geometry. In this work the standard Fortran code has been modified to be more efficient and easy to customize: most of the critical geometry data used by GEANT to construct the BCAL module have been transferred into ASCII data cards. New functionality has been also added: simulations of modules with different lead sheet thickness and/or different lead sheet thickness for the inner layers versus the outer layers can be done easily by making appropriate changes to the data card.

Two different ways were used to implement the geometry in GEANT3. In the first, the glue boxes were approximated by trapezoids between the fibres and in the second, strips of glue were placed "inside" the lead with the fibre volumes on "top". To distinguish them, the first will be termed *traps* (Figure 4.3a) and the second *strips* (Figure 4.3b).

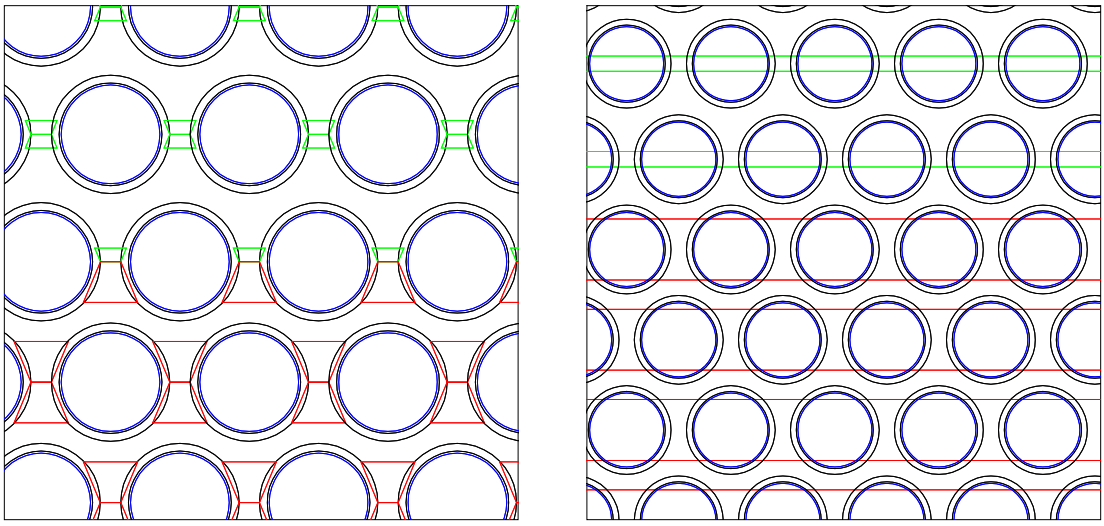

(a) *traps* implementation (b) *strips* implementation

Figure 4.3: Different implementations of the hybrid geometry.

4.3 Results

Simulations have been carried out for all geometries listed above, at various angles with respect to the beamline, and at several energies. The goal was to extract the longitudinal shower profile shape, the energy resolution (σ_E/E) and the fractional energy deposition (f) for each geometry. The two different implementations of the lead-fibre-glue matrix yielded the same results and for that reason the 'traps' implementation results are not shown. This also adds to the clarity of the graphs.

4.3.1 Longitudinal Shower Profile

The parametrized longitudinal development of electromagnetic shower describes the shower reasonably well [22] when the incident photon energy is larger than 1 GeV. If the depth in the material, expressed in radiation length units, is $t = x/X_0$[5] and the energy of the incident particle is E_0 then

$$\frac{dE}{dt} = E_0\, b\, \frac{(bt)^{a-1}\, e^{-bt}}{\Gamma(a)} \tag{4.3}$$

describes the evolution of the electromagnetic cascade in the material. The parameters a and b depend on the nature of the incident particle and the type of the absorbing material. The depth in the material, where the shower maximum occurs, depends on the incident particle's energy E_0 and the critical energy E_c

$$t_{max} = ln\frac{E_0}{E_c} + t_0 = \frac{a-1}{b}, \quad t_0 = \left\{ \begin{array}{ll} +0.5 & \text{for photons} \\ -0.5 & \text{for electrons} \end{array} \right\} \tag{4.4}$$

In the case of the absorbing medium being a compound (made of different ma-

[5] x is distance measured in cm.

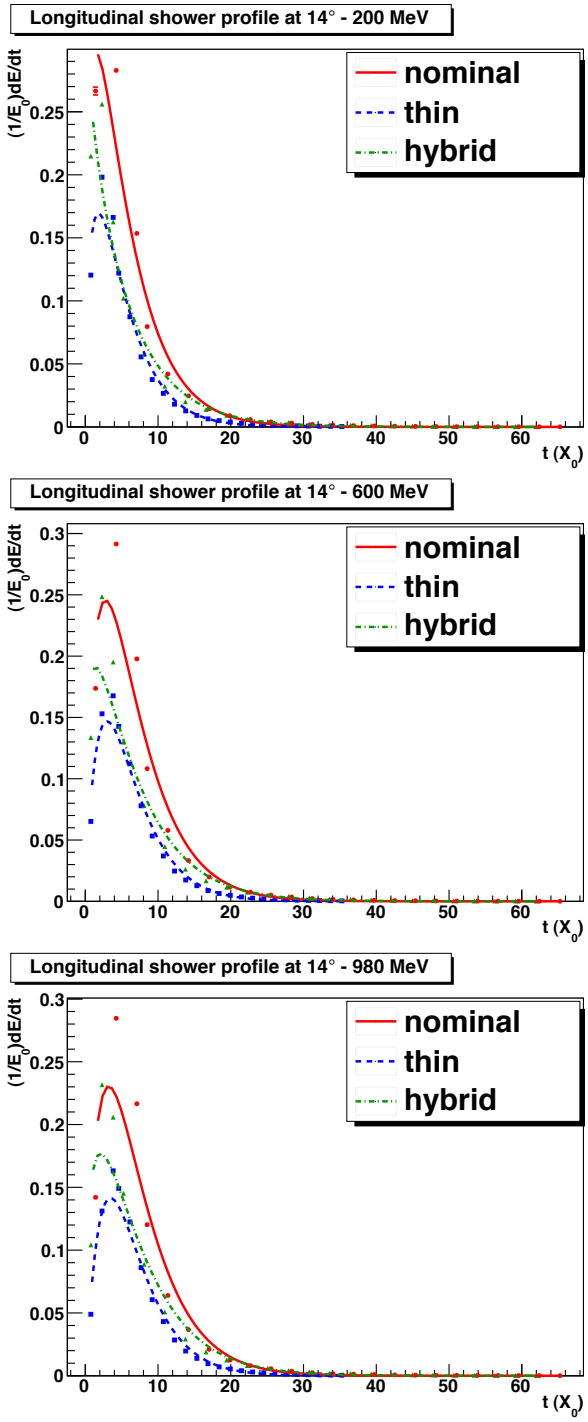

Figure 4.4: Longitudinal shower profile at 14° for different geometries. The data points correspond to the Monte Carlo results, fitted with Equation 4.6 represented by the lines. Detailed discussion is given in the text.

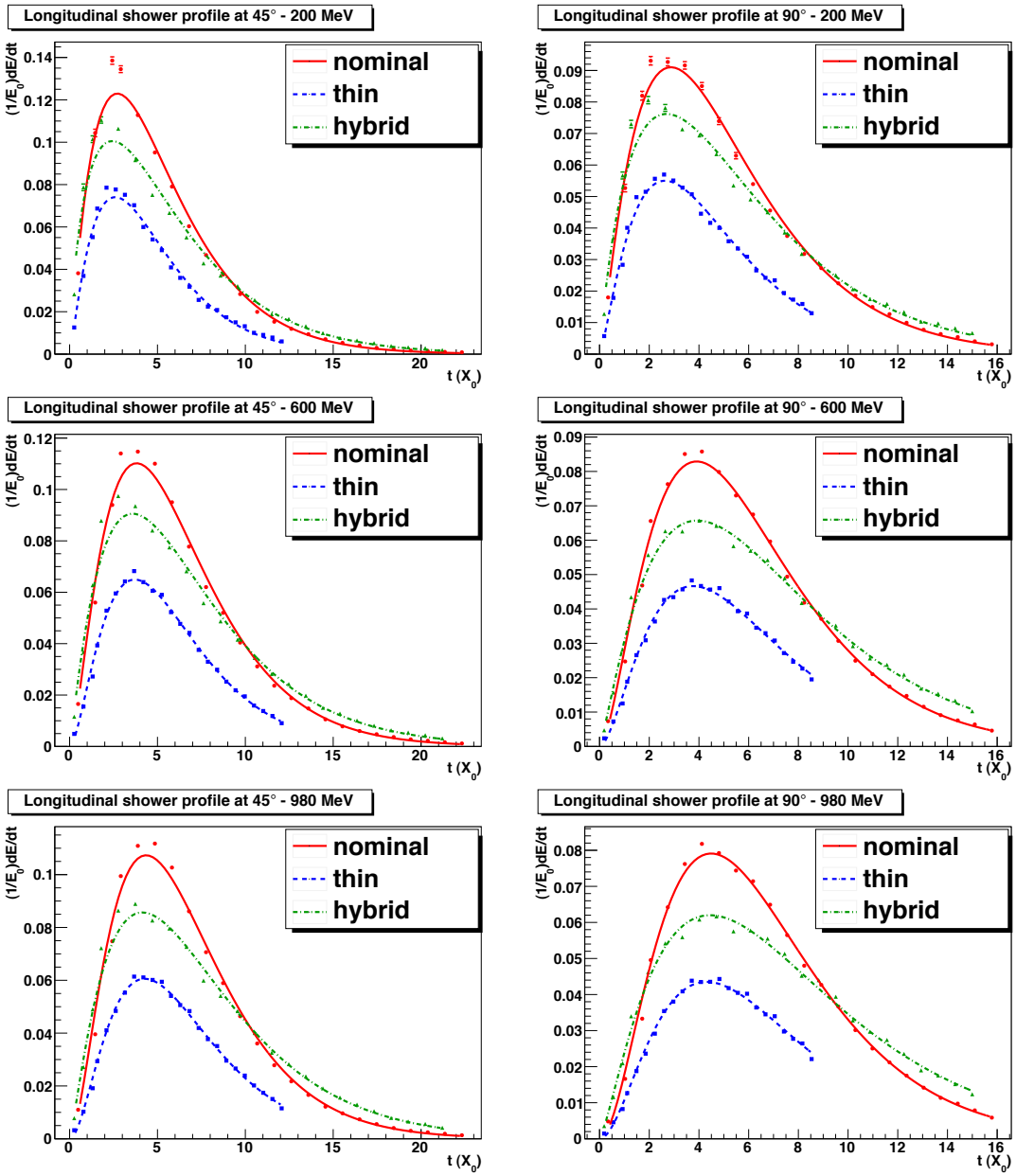

Figure 4.5: Longitudinal shower profile at 45° and 90° for different implementations and geometries. The data points correspond to the Monte Carlo results, fitted with Equation 4.6 represented by the lines. Detailed discussion is given in the text.

terials), the critical energy depends on the Z_{eff} of the compound according to the Rossi formula [24]:

$$E_c = \frac{610MeV}{Z_{eff} + 1.24} \tag{4.5}$$

Equation (4.3) then, with the appropriate parameters, describes the shape of the longitudinal shower profile in the lead-fibre-glue matrix.

The longitudinal shower profile for different angles of the incident photon with respect to the beam direction, as well as different incident photon energies, are shown in the set of graphs in Figures 4.4 and 4.5. Simulations at 90° were chosen because normal incidence is a standard for validating the simulation. At 14°, the direction of the incident photons points to the forward outer end of the BCAL module, where the majority of high energy particles is expected. The 45° angle was chosen as an intermediate angle.

The data points in each case have been fitted with the function

$$\frac{1}{E_0}\frac{dE}{dt} = c\,b\,\frac{(bt)^{a-1}\,e^{-bt}}{\Gamma(a)} \tag{4.6}$$

which is based on the assumption that the simulation data will be reasonably well described by Equation 4.3. Indeed all simulated profiles shown are for the energy deposited in the lead-fibre-glue matrix and exhibit the characteristic shower profile shape. At smaller angles, the depth in the module that the shower develops increases. At the shallow angle of 14° the lower energy particles deposit almost all of their energy in the first segment of the module. This explains why the fitted function does not describe the shower development as well as it does for the 90° or the 45°. Finer segmentation in the radial direction, for the inner parts of the module, would provide better results as there would be more data points to fit in that region.

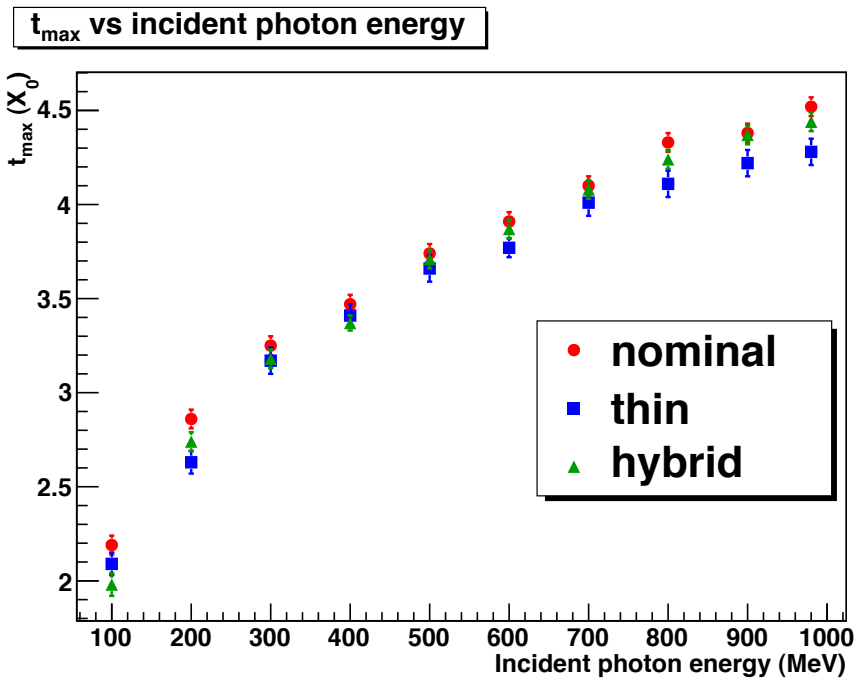

Figure 4.6: t_{max} versus incident photon energy. The shower maximum occurs deeper in the module as the energy of the incident photon increases. The same data plotted versus distance in cm would appear dramatically separated for the three configurations, a fact that illustrates the usefulness of plotting versus t instead of x.

The abrupt termination of the thin geometry data and fit, corresponds to the end of the matrix, 8.90 X_0 (see Table 4.3), and likewise for the hybrid simulations at 14.51 X_0 and nominal at 16.47 X_0. The hybrid curves cross over the nominal ones and this simply reflects the differing density and thus shower profiles. Note that both configurations contain most of the showers and the integrals under those curves are approximately equal.

The dependence of t_{max} (determined by the Monte Carlo simulation) on E_0 is shown in Figure 4.6, where, as expected, the shower maximum occurs deeper in the module as the energy of the incident photons increases. As the electomagnetic density of the module increases, so does the total energy deposited in the module. The more dense nominal geometry contains more of the shower's energy than the hybrid or the thin geometry.

4.3.2 Energy Resolution

Energy resolution is defined as the ratio of the width of the distribution, divided by the distribution itself (σ_E/E) and it can be given as the sum in quadrature of three terms:

$$\frac{\sigma_E}{E} = \frac{a}{\sqrt{E(GeV)}} \oplus b \oplus \frac{c}{E} \tag{4.7}$$

The first term is referred to as the stochastic term due to the fact that it is dominated by the shower fluctuations. Since the calorimeter is constructed of layers of fibres interleaved with lead, the number of shower particles reaching the sampling medium (fibres) has a stochastic behaviour, and as a result the energy deposited in the sampling medium inherits this stochastic behaviour. Increase of the sampling-medium volume reduces fluctuations and improves the resolution. On the other hand, this modification leads to a "lighter" (less dense) calorimeter with compromised abil-

ity to stop energy leaking out the back. In order to achieve the best energy resolution possible, within a given region of the incident particle's energy, the sampling medium weight must be optimized.

The second term, called the floor term, is energy independent. It reflects the spread of the deposited energy distribution due to factors such as irregularities (non-uniformities) of the lead, glue, fibre matrix, shower leakage and non-uniformities in the detection process.

Finally, the last term is called the noise term and depends mostly on electronics noise in the experiment. If a high signal-to-noise ratio is achievable, the noise term is negligible (especially when added in quadrature). In this work, however, there are no electronics involved since there are only simulation data and therefore the noise term was set to zero.

The function used to fit the graphs is:

$$\frac{\sigma_E}{E} = \frac{a}{\sqrt{E(GeV)}} \oplus b \tag{4.8}$$

For photons at normal incidence, the nominal geometry results are in agreement with past simulations [25], including the decrease of the floor term at forward angles and this lends confidence to the method and simulation code used in this work. Additionally, the resolution at 90° for the nominal and thin lead geometries behaves as expected, with the former having a higher $\frac{1}{\sqrt{E}}$ term and lower floor term than the latter. This is understood in the sense that the latter has a higher fibre volume and thus collects more of the deposited energy, which improves the stochastic fluctuations ($\frac{1}{\sqrt{E}}$ term), whereas its reduced density leads to increased shower leakage and thus worse floor term.

At 45° the stochastic term is improved for all geometries compared to the 90°

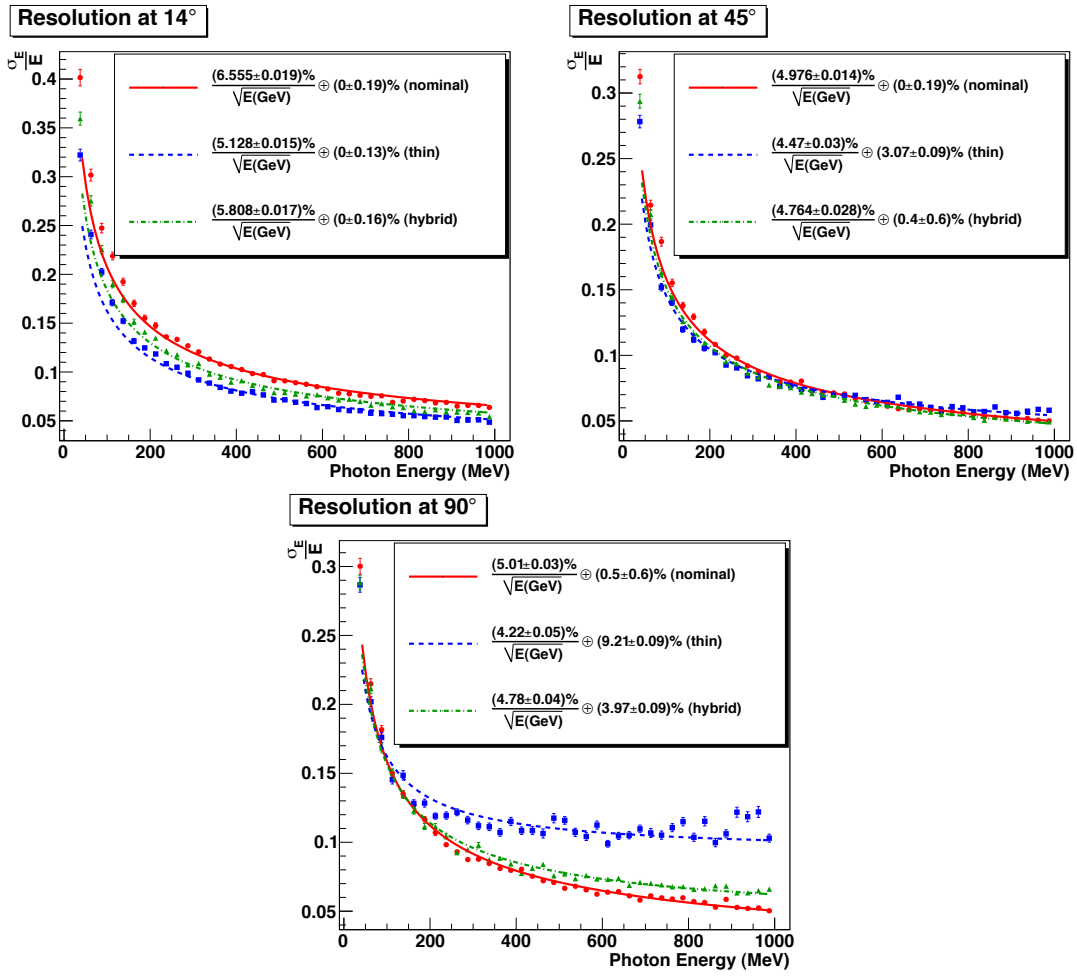

Figure 4.7: Energy resolution as a function of incident photon energy at $14°, 45°$ and $90°$ for all three geometrical configurations (nominal, thin and hybrid).The points are simulated data whereas the lines represent fits to the data using Equation 4.8.

as a result of the improved ability of the module to contain the electromagnetic shower at that angle. The floor term is expected to be lower than the 90° case because of the lesser number of layers intercepted by the shower particles. Overall, the energy resolution is improved at 45° when compared with the 90° simulations for all geometries. Note how at 45° all geometries are very close as far as resolution is concerned. The nominal geometry resolution has improved but the thin and hybrid have improved more as an advantage of their increased *"sampling fraction"*.

At 14° the situation has changed dramatically. All geometries show worse resolution, which is a manifestation of the increased shower leakage from the front of the module[6]. The shower path at 14° is long enough to eliminate leakage from the back of the module and the relative improvement in the resolution, due to the increased sampling fraction of the thin and hybrid geometry, is apparent as is also expected. The floor term at 14° is significantly lower, reflecting the fact that less layers are intercepted and thus uncertainty due to structure irregularities is decreased.

4.3.3 Sampling Fraction

Sampling fraction is defined as the fraction of the energy that is deposited in the sampling material (here scintillating fibres) over the total energy deposited in the module:

$$f = \frac{E_{scifi}}{E_{mod}} \tag{4.9}$$

It can also be expressed as the ratio of the energy deposited in the sampling material over the energy of the incident particle:

$$f_\gamma = \frac{E_{scifi}}{E_\gamma} \tag{4.10}$$

[6]For results on the 14° shower leakage the reader is referred to Appendix A, on page 78.

with $f_\gamma < f$ since $E_{mod} < E_\gamma$, owing to energy leakage outside the calorimeter volume.

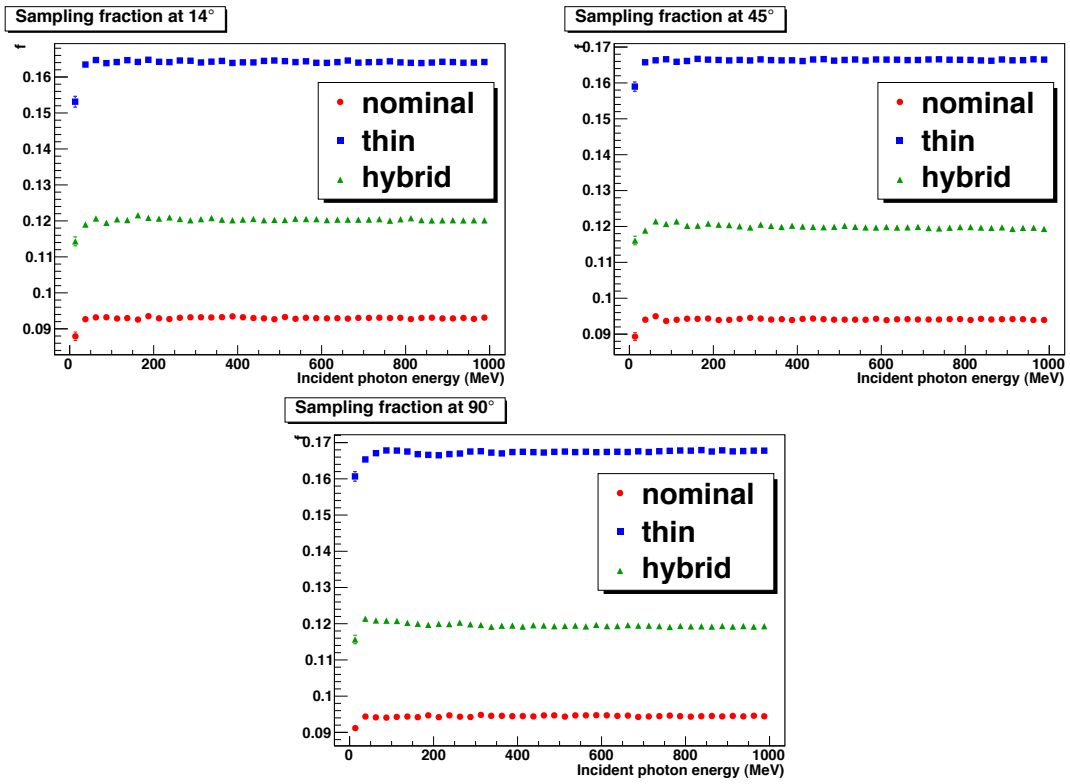

Figure 4.8: Sampling fraction versus incident photon energy for different angles. The sampling fraction is approximately constant for the majority of the energy spectrum.

The sampling fraction, plotted as a function of the incident photon energy, is shown in Figure 4.8. The sampling fraction for the nominal geometry is constant, except for the low energy region, and its shape is in general agreement with past studies [22, 25], although the magnitude is less in this work (9.5% instead of 11.5% in [22, 25]). This is expected by refining the SciFi volume to include the insensitive[7] two layers of cladding. This difference is discussed below. The thin and hybrid geometry lines are higher than the nominal reflecting the increased fibre volume.

[7]Insensitive in this context has the meaning of not contributing to the energy deposited in the fibres.

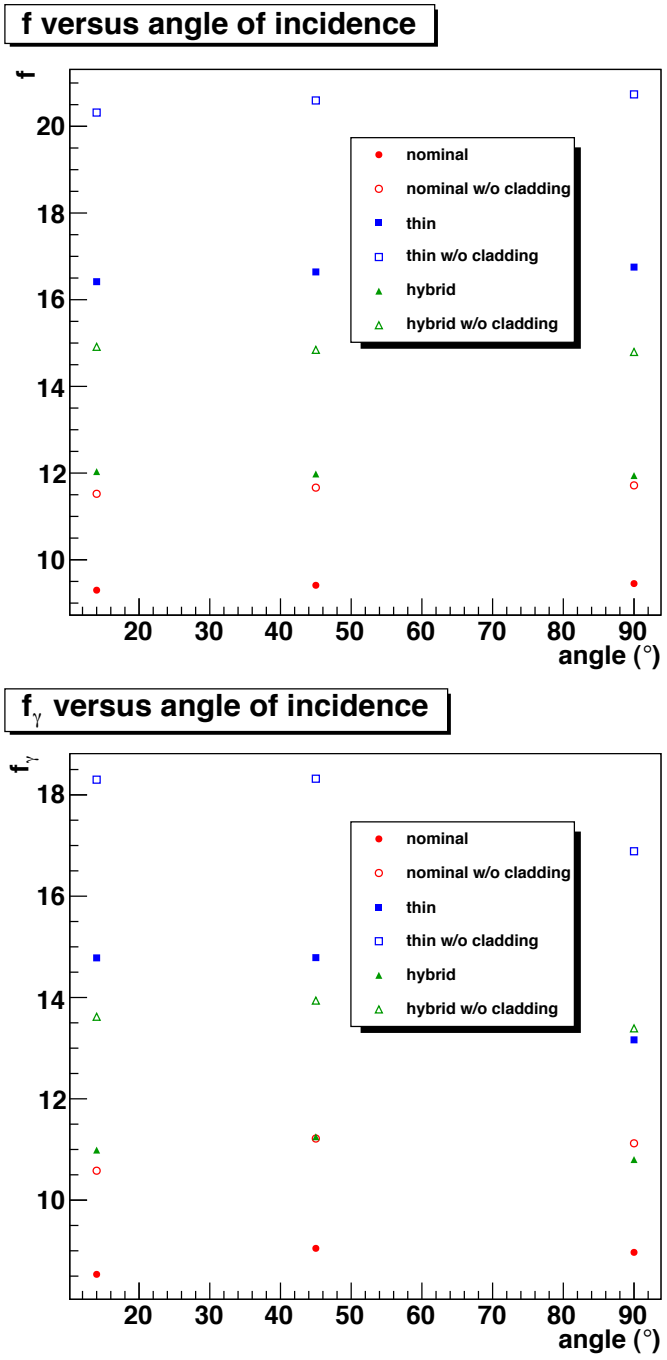

Figure 4.9: Sampling fraction versus angle of incidence. f is almost constant for the same geometry. f_γ tends to be lower as E_0 increases and the thickness decreases. This is due to the energy leaking out the back of the module.

This increase verifies the intended goal of these geometrical configurations.

The sampling fraction is somewhat lower than past studies. This is understood based on two important differences in the two sets of simulations. The first is due to the difference in the geometrical configuration, namely due to the radial pitch being changed from 1.22 mm to 1.24 mm, in order to better approximate the actual pitch value of the prototype module, but only contributes modestly to the degradation. The second is the reduction of the fibres core volume due to the addition of cladding.

Cladding represents 5% of the total diameter of the fibre, as specified in manufacturer's specifications, and accounts for 19% of the volume of the fibre. Therefore, in the simulations carried out the sampling material is less in volume than past simulations, where the total diameter of the fibre was contributing to the sampled energy. This reduction in the sampling material affects the sampling fraction as shown in Figure 4.9. The sampling fraction without cladding and with cladding is termed f_{wo} and f_w, respectively. From Figure 4.9 $f_{wo} \approx 11.7\%$ and $f_w \approx 9.5\%$ approximately. There is a decrease in the sampling fraction of

$$\frac{\Delta f}{f_{wo}} = \frac{f_{wo} - f_w}{f_{wo}} \approx 19\%$$

reflecting the decrease of the volume of the sampling material. The sampling fraction, without the cladding, is approximately $\sim 11.7\%$ and is in agreement with past simulations of the BCAL [25]. However, the figure of $\sim 9.5\%$, in this work more accurately represents the actual BCAL configuration because of having taken the cladding into account.

4.4 Energy leakage

The energy leakage out the calorimeter volume for normal incidence[8] and all radial pitch configurations is shown in Figure 4.10. The different points correspond to energy leaking out from different faces of the module. Front and back refers to the inner and outer faces of the module, respectively, with respect to the radial direction. Leakage from the ends refers to the energy leaking out from the faces of the module along the direction of the beam, where photo sensors will be placed. Leakage from the sides refers to the faces of the module that will be in contact with it's nearest neighbour modules. As the latter will be recovered in adjacent modules during the experiment, it was not included in the leakage sum. Indeed, total energy leakage refers to the sum of all energy leaking out the module from front, back and ends.

For all incident photon angles, irrecoverable energy leak occurs mostly from the back of the module. The module's radial thickness was previously calculated at normal incidence and shown in Table 4.3. As the X_0 thickness of the module decreases, due to the change in pitch, more energy leaks from the back. The leakage through the back increases monotonically, following the evolution of t_{max}, which means that the shower develops further inside the module along the radial direction. It is interesting to note that the amount of energy leaking out from the sides is of the magnitude as the energy leaking from the back, although the former will be recoverable in the experiment. R_M for the thin lead geometry is 5.57 cm, while for the nominal configuration is 3.54 cm. For the thin geometry, R_M is larger than half the width of the module, which explains the increased leakage from the sides.

There is little energy leaking out the front face of the module, in all configurations, but it tends to be larger at lower energies and smaller angles. The generation

[8]See appendix A in page 78, for energy leakage for angles other than normal.

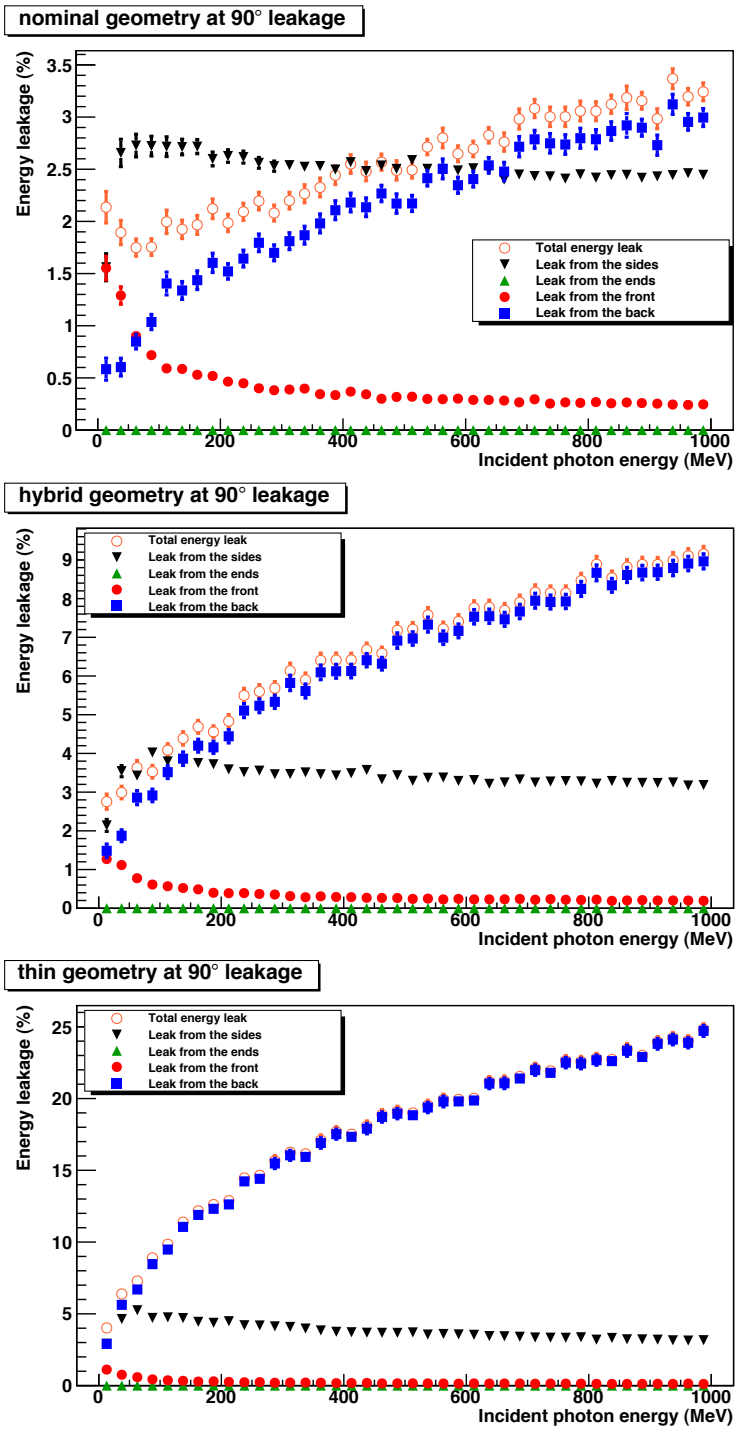

Figure 4.10: Energy leakage versus incident photon energy at 90° for all geometries simulated. Energy leakage from the sides is plotted but not added to the total energy leak curve. As expected, the less dense the geometry, the larger the leak is. The leakage out the ends is consistent with zero in all cases.

of secondary particles in the converter (here lead), depends on the incident photon energy but has a stochastic behaviour. Low energy particles have increased probability of interaction with only a few layers of lead before the secondary particles drop below the energy threshold for generation of secondaries. Furthermore, there is increased probability of low energy particles to back scatter and end up leaving the module out the front.

The energy leaking out the ends of the module is low, even at the 14° angle of incidence, primarily due to absorption in the inner layers of the module before the shower development reaches the rear forward corner.

4.5 Summary

The nominal geometry has been tested once again with the GEANT-based, standalone Monte Carlo. The critical parameters such as energy resolution and fractional energy deposition have been extracted and are in qualitative agreement with past simulations.

The addition of cladding to the fibres resulted in a significant reduction of the sampling fraction. A new geometry with thinner lead sheets and fibre pitch of 1.11 mm was simulated and it lead to increased sampling fraction and higher energy resolution. The energy leakage, though, is significantly increased. Such a choice of geometry would be beneficial, if the energy of the incident particles was expected to be low. However, under experimental conditions, the BCAL will be exposed to photons with energies between 40 MeV and 3.5 GeV. The reduction in effective radiation lengths that the thin lead geometry confers would entail a serious degradation in energy resolution over most of that range, which would compromise the event reconstruction and amplitude analysis. As such this study has shown that the thin lead geometry

is not a viable option for GlueX.

The hybrid geometry, on the other hand, afforded more light production in the crucial inner layers, while preserving the radiation lengths and therefore not compromising the energy resolution significantly. Nevertheless, this option was also not pursued for two reasons: a) it would introduce a non-uniformity between inner and outer layers, which adds to the complexity of reconstruction and somewhat degrades the overall performance, but mostly due to b) the GlueX timetable, which by that time, did not allow for the R&D required in swaging thinner lead and "stitching" the thin and nominal lead sections together. Therefore it was decided within GlueX to not pursue either the thin or the hybrid designs further.

Finally, since the initiation of this study it has been decided that the SiPMs will be thermally stabilized, thus reducing the dark current and improving detection of low energy particles near thresholds thus increasing the acceptance of the BCAL. This improvement is significant enough to forego a change in the geometry of the calorimeter itself, which is considerably harder to achieve successfully.

Chapter 5

Hall-B Beam Test Data Analysis

5.1 Module Description

The first 4-m-long prototype BCAL module, termed Prototype-1, was constructed in 2004 by University of Regina personnel at the University of Alberta. Its cross section is rectangular, unlike the trapezoidal cross section of the production modules, to minimize unnecessary machining costs and to better contain the electromagnetic shower during the beam tests. It is 400 cm long with a cross-sectional area of 13 $cm \times 23$ cm. Prototype-1 incorporated 1 mm diameter, blue-emitting, double clad scintillating fibres, made by PolHiTech[1], type PHT-0044, while the production modules incorporate Kuraray[2] double-clad fibres of the same diameter. The fibre's core diameter is 0.96 mm while the rest is cladding. The PolHiTech fibres have a maximum emission peak at 420 nm [26] wavelength and 350 cm attenuation length[3].

Figure 5.1 is a sketch of the geometry of the lead, scintillating fiber and glue matrix. The distance between the centres of the fibres between adjacent layers is

[1]PolHiTech SRL, 67061 Carsoli, Italy (`www.polihitech.it`)
[2]Kuraray America Inc. 4 Park Plaza Suite 530 Irvine, CA 92614 U.S.A (`www.kuraray-am.com`)
[3]Values quoted by the manufacturer.

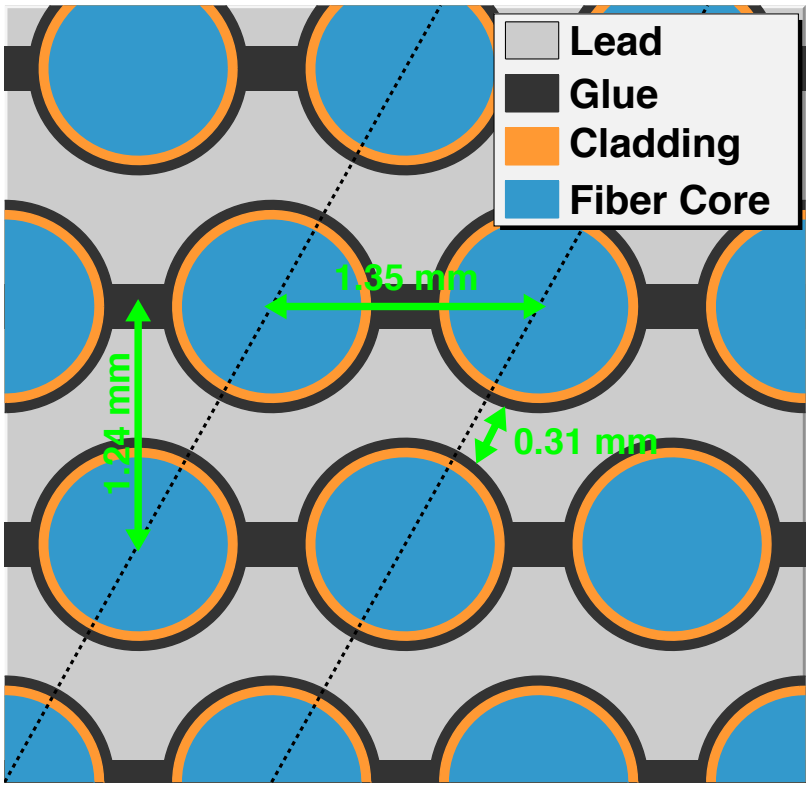

Figure 5.1: Internal structure geometry properties of Prototype-1. The distance between layers of fibres (radial pitch) is 1.24 mm as opposed to the 1.22 mm of the production modules, while the azimuthal pitch is 1.35 mm.

1.24 mm, as opposed to 1.22 mm for the production modules. The distance between the fibres (center-to-center) of the same layer is 1.35 mm as this is dictated by the mechanical (plastic deformation) apparatus. The composite has a Pb:Scintillating fibre:Glue ratio of 37:49:14, an overall density of 5 g/cm^3 and a radiation length of 1.5 cm.

5.2 Goals

In 2006, the prototype module was shipped to the Jefferson Lab[4] for a beam test. The primary goals of the beam test were to extract the energy and timing resolutions and the number of photoelectrons and to compare with past Monte Carlo studies. Secondary goals were to extract the effective speed of light in the fibres and the attenuation length. The latter were reported previously [27, 28].

From the KLOE experiment [16], the energy resolution has been shown to be close to $5.4 \pm 0.03/\sqrt{E(GeV)}$ with a negligible floor term. The timing resolution is expected to be around $56 \pm 0.03/\sqrt{E(GeV)}\, ps$.

5.3 The Hall-B tagged photon beam

For these tests, an electron beam of 675 MeV/c momentum at Hall-B in Jefferson Lab, was used. To produce the photon beam, the electron beam was incident upon a thin tungsten target (the "radiator"). The radiator was placed just upstream from a magnetic spectrometer (the "tagger"). This setup provided a photon beam via the electron bremsstrahlung mechanism. Electrons from the electron beam were decelerated by the electromagnetic field of a nucleus (radiator) and emitted an energetic

[4]Thomas Jefferson Lab National Accelerator Facility, Newport News, VA 23606 (`www.jlab.org`).

photon (gamma ray). Since the energy of the electron was known from the beam characteristics (E_0), a measurement of the energy of the scattered electron (E_e) provided the energy of the photon (E_γ):

$$E_\gamma = E_0 - E_e \tag{5.1}$$

Immediately downstream of the target was the magnetic spectrometer which provided an accurate measurement of the scattered electron's momentum (and therefore energy E_e) and also timing information used for the trigger. To address these two tasks the magnetic spectrometer utilizes two kinds of scintillators placed into two different planes: the E-plane (E for energy) and the T-plane (T for time). The E-plane (see

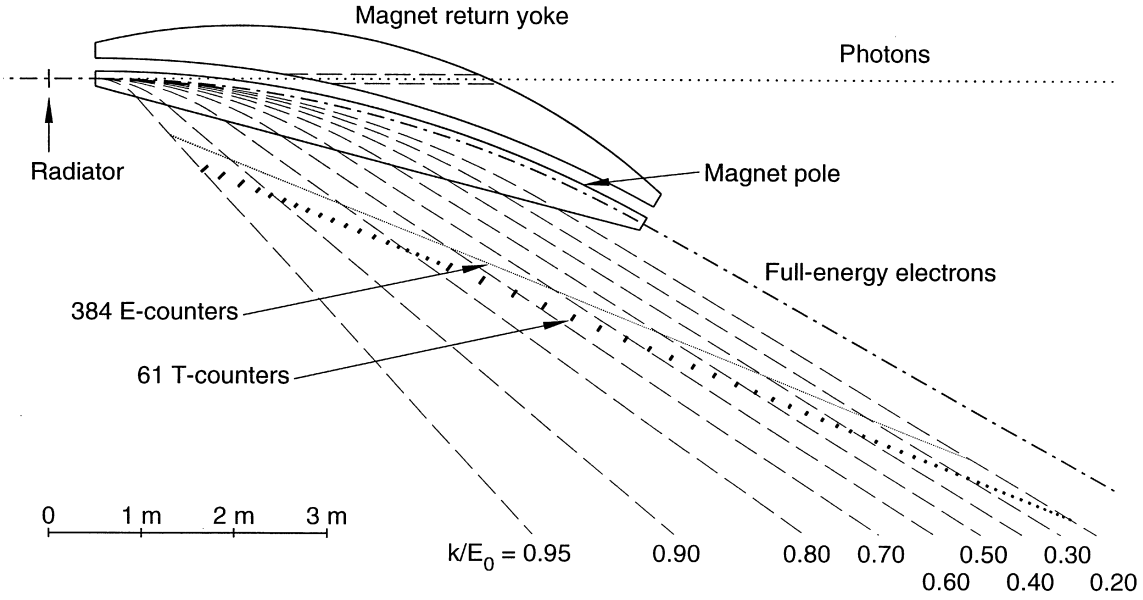

Figure 5.2: The magnetic spectrometer of Hall-B. The E-plane (E-counters plane) and the T-plane (T-counters plane) can be seen, as well as the trajectories of scattered electrons of different momenta.

Figure 5.2) consists of 384 plastic scintillators, called E-counters, 20 cm long and 4 mm thick and with variable width so that they can subtend almost constant energy

intervals of $0.003E_0$. The E-counters physically overlap, thus creating 767 separate photon energy bins by combining signals from adjacent E-counters. This setup leads to an overall energy resolution of the photon beam in the order of $10^{-3}E_0$ [29].

The T-plane consists of 61 counters, called T-counters, 2 cm thick each. The T-counters are separated into two groups, with the first group of 19 narrower counters spanning the photon energy range from 75% to 95% of the electron beam and the remaining group of 42 counters spanning the range from 20% to 75% of the electron beam energy. This setup assures that the counting rate in each detector remains approximately constant within each group [29].

The photon beam was collimated by a 2.6-mm-radius collimator. The result was a 2 cm radius beam spot on the module, nearly 33 m downstream. This relatively small radius contributed to the accuracy of timing measurements and facilitated the extraction of the timing resolution and ultimately the position resolution.

5.4 Module setup

The module was placed in front of the Hall-B downstream alcove. The size of the module, with the read-out system and cables, was larger than the width of the alcove and an additional platform had to be installed in front of the alcove so that measurements with the module perpendicular to the beam would be taken, as shown in Figure 5.3. Physical access to the hall was required to change the position of the module for the measurements perpendicular to the beam, at positions along the length of the module from -100 cm to +25 cm relative to the centre of the module (0 cm). The module was mounted on a remote controlled cart which was designed to withstand the module's weight and also could be rotated remotely for measurements at different angles. When inside the alcove, rotation was limited to less

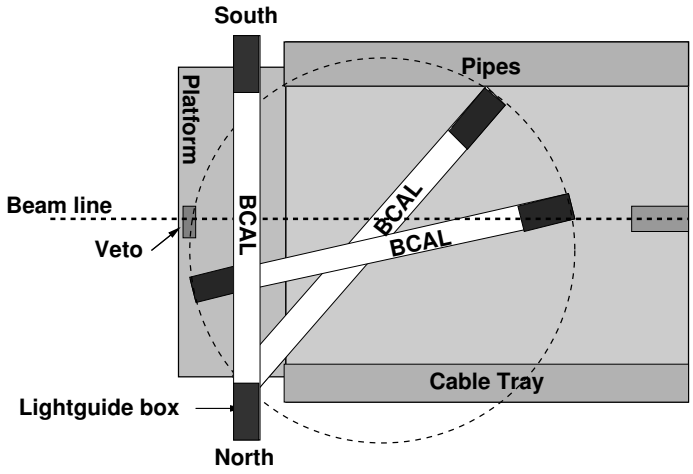

Figure 5.3: A sketch of the various positions of the module relative to the alcove as well as the beam line used for the beam test requirements. The platform in front of the alcove allowed the module to be illuminated by the beam perpendicularly spanning from -100 cm to +25 cm. When inside the alcove, measurements were taken for angles less than 40° because of the relative sizes of the module and the alcove.

than 40° because of the relative size of the module and the alcove. The combination of different positions and angles used for acquiring data for the beam test can be seen in Figure 5.4, denoted by the triangular markers.

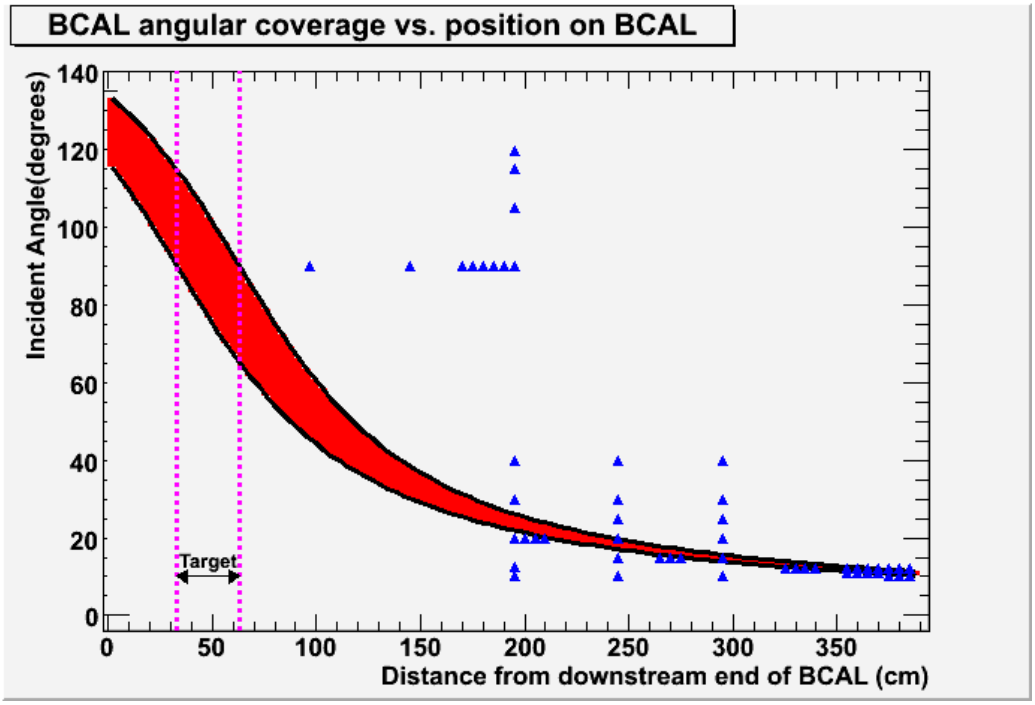

Figure 5.4: Angle versus position of the measurements taken for the beam test. The blue triangles indicate measurements taken at the specific angle and position. The red area represents the relation between angle and position for photons in the actual GlueX experiment.

5.5 Read-out and electronics

A schematic representation of the read-out used for the beam test is shown in Figure 5.5. Each end of the module was divided into 18 individual read-out segments in a 3×6 fashion. Each segment covered an area of $3.81 \times 3.81\, cm^2$. Although silicon photo-multipliers will be used for the read out of GlueX, for the beam test conventional photo-multipliers were used because of their well known behaviour and

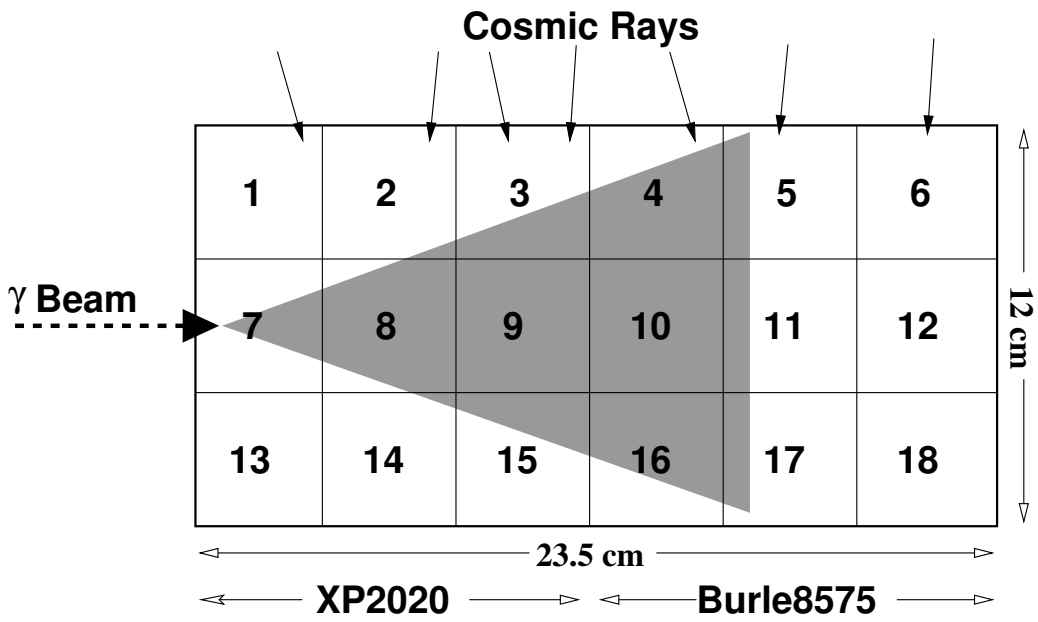

Figure 5.5: A schematic representation of the segmentation used for the beam test on each end of Prototype 1: 18 detection segments in a 3×6 fashion. The inner three layers of readout cells (with respect to the beam entry point) were read by XP2020 photo-multipliers while for the outer three Burle 8575 were used. The grayed area is only a sample sketch of the shower as it develops in the BCAL module and not an accurate representation of it.

also because the SiPM devices were still in the R&D stage.

Three columns of XP2020[5] PMTs were used to read out the upstream-most cells (with respect to the beam's direction) because of their better timing characteristics as opposed to the available Burle 8575[6] that were mounted on the outer segments.

Acrylic light-guides with a square cross section and a 45° mirrored surface that redirected the light at 90° relative to its original direction, were employed to transport the light to the photo-multipliers, which were oriented perpendicular to the fibres (upright). The photo-cathode of each PMT was coupled to the face of the light guide using a silicon cookie[7]. The silicon cookie ensures that light losses due to reflection, as a result of the difference in the indeces of refraction, are minimized. The readout system was enclosed in a light-tight steel box to shield the PMTs from ambient light and from magnetic fields.

The logic diagram of the electronics used for the beam test at Hall-B is shown in Figure 5.6. The signal from each photo-multiplier was split into two signals. One was sent straight to the CAEN V792 ADC unit[8], which converts the analog signal to a digital signal depending on its amplitude (Analog to Digital Converter). The digital signal is then ready to be recorded. The sum of the signals from the PMTs went through a second discriminator whose threshold was set so that output would be produced only if at least four PMTs had generated a pulse. The signal of the sum from both ends of the module with the MasterOR signal from the tagger was used as the event trigger. A LeCroy 1877[9] TDC and a CAEN 1290[10] TDC were used for time to digital conversion for the signal of the E-plane (Ephoton) and the T-plane

[5] www.photonis.com/upload/industryscience/pdf/pmt/XP2020UR.PDF

[6] www.burle.com/cgi/byteserver.pl/pdf/8575B.pdf

[7] ELJEN Technology (http://www.ggg-tech.co.jp/maker/eljen/list.html)

[8] http://www.caentechnologies.com/nuclear/Printable/data_sheet.php?mod=V792&fam=vme&fun=qdc

[9] http://www.lecroy.com/lrs/dsheets/1877.htm

[10] http://www.caen.it/nuclear/product.php?mod=V1290N

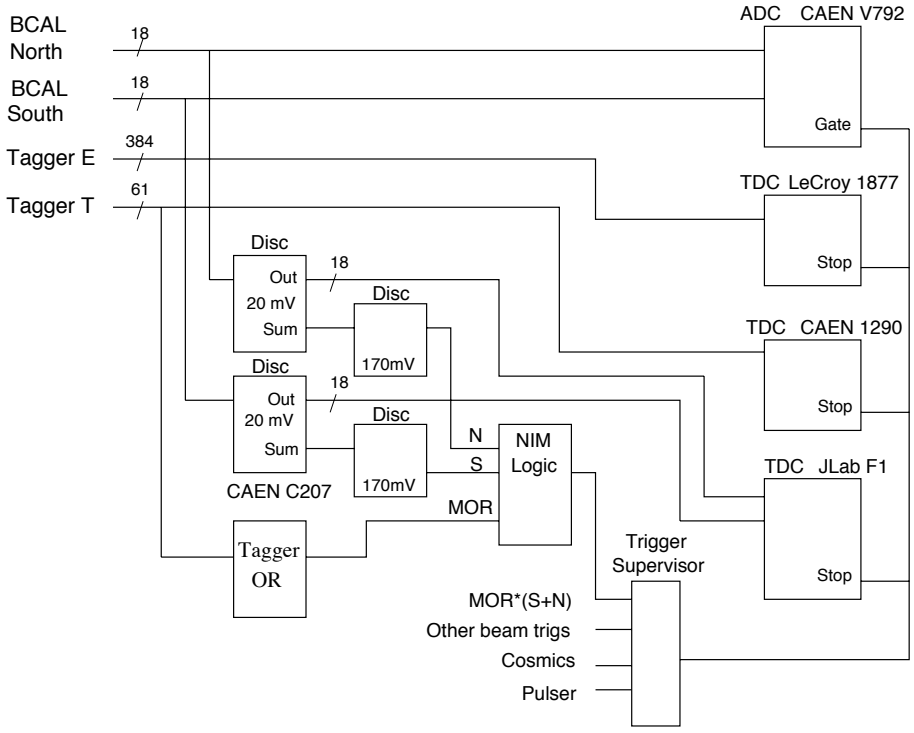

Figure 5.6: Logic diagram of the electronics used for the beam test at Hall-B. The trigger was formed by the tagger MasterOR signal and the sum of the photo-multiplier signals from North and South. The setup was such that a trigger event would occur if at least four photo-multipliers from either side of the module had generated a pulse.

(tphoton) of the tagger, respectively.

5.6 Data quality tests

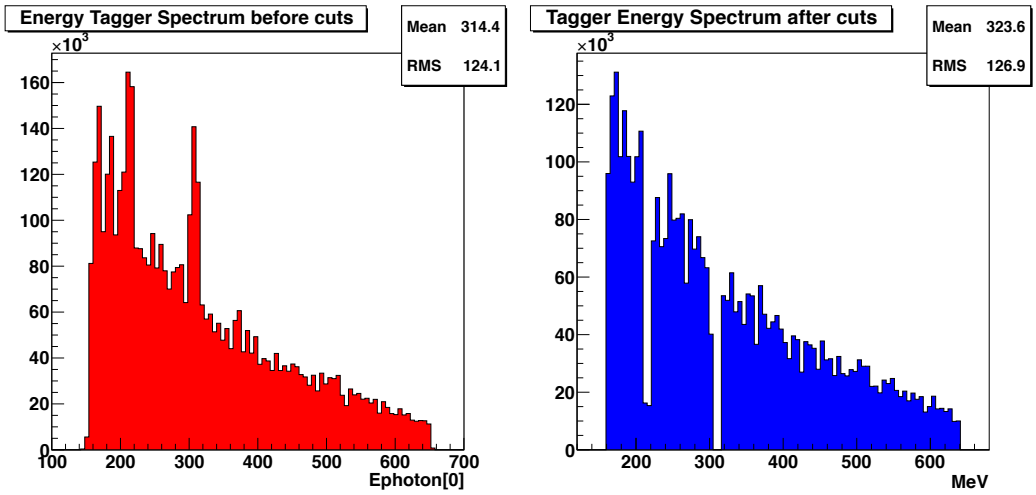

(a) (b)

Figure 5.7: The cuts on the tagger energy spectrum. Two bands of 10 MeV width each were discarded from the tagged photon energy spectrum. More information is given in the text.

One expects the tagger energy spectrum to reflect a smooth and continuous distribution. However, the energy spectrum distribution at the beam test was not smooth, probably indicating misbehaviour of some energy counters (Figure 5.7a) resulting in two peaks at around 220 MeV and 310 MeV respectively. Various tests were performed to determine if there was any way to exclude these two regions based on evidence in Prototype 1. The results didn't show any physics-driven correlation leading to their exclusion via vertical cuts. The final energy spectrum after applying the cuts is shown in Figure 5.7b.

The timing spectrum after the cuts were applied is shown in Figure 5.8. The structure is most probably a result of jitter of the T-counters. All analysis was

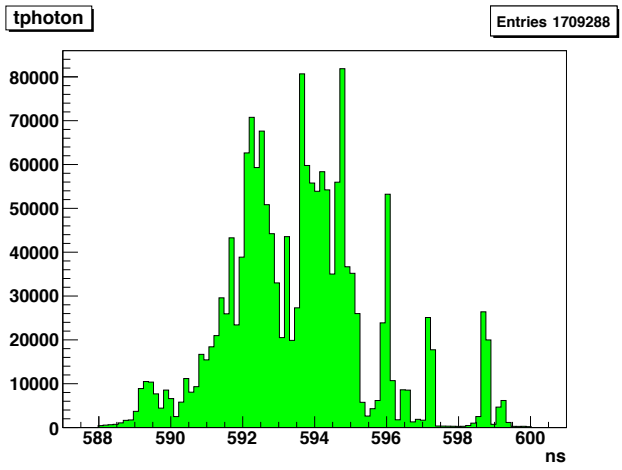

Figure 5.8: The tphoton spectrum after applying the cuts. Events outside the 594 ± 6 ns range were excluded from the analysis. The timing window chosen for the analysis was shown to be the narrowest possible without sacrificing any of the energy spectrum.

carried out within a narrow timing window approximately 12 ns wide centred at 594 ns. Investigation of the correlation between the timing spectrum and the energy spectrum showed that the chosen timing window is the narrowest possible without sacrificing any of the energy spectrum.

Other analysis cuts used were:

- In order to consider the most simple cases, events where more than one photon per event (double hits) were detected were excluded by setting Nphotons=1.
- Only events coming from the beam were considered, therefore all the events that had set the trigger bit for cosmic or pulser origins were excluded.
- The data used had the ADC pedestal (effectively zero energy in spectrum) subtracted and therefore some of the ADC values were negative. This effect was a concern for readout cells that the energy deposition is small, and it was addressed by requiring the central cells to have $ADC > 0$.. Thus, it is certain that only events with sufficient energy deposition, were considered.

5.7 Results

In order to extract the energy deposition in the BCAL from the data at hand, an offline calibration of the ADC signals was required. Gain calibration accounts for the difference in the gain of the different PMTs used and also for the differences in the high voltage supplied to them. After the gain calibration, an overall factor was calculated to convert the ADC channel signal to energy units (MeV).

The calibration procedure had already been carried out for the setup used to obtain the data in this work [21]. This means that the gain calibration constants, as well as the overall ADC to MeV factor, have been taken to be the same in this work

as in past studies. However, past studies were carried out for a different subset of the data and it will be interesting to investigate and compare these in the future.

5.7.1 Energy resolution

The data used to extract the energy resolution are summarized in table 5.1 The

Table 5.1: Run number 2334 with z=0 cm and $\theta = 90°$ has been analysed extensively during the analysis development stage and is referred to as the "golden run". For that reason it was used as a reference for the results in this work.

Run #	θ (°)	z (cm)
2334	90	0
2388	40	-100
2389	30	-100
2390	25	-100
2391	20	-100
2392	15	-100
2393	10	-100

available tagger energy spectrum (Figure 5.7b) was divided into 30 energy bins of equal width. The number of the bins was chosen so that the statistics in each bin would be adequate and also to keep the bin width small enough to have a reasonable error bar on the tagger energy.

The reconstructed energy termed E_{cal} is given by Equation 5.2.

$$E_{cal} = \sqrt{\left(\sum_{1}^{18} ADC_{left}\right) \times \left(\sum_{1}^{18} ADC_{right}\right)} \tag{5.2}$$

The ADC signals from all left PMTs and all right PMTs were summed and the geometric mean of the sums was used as the reconstructed energy.

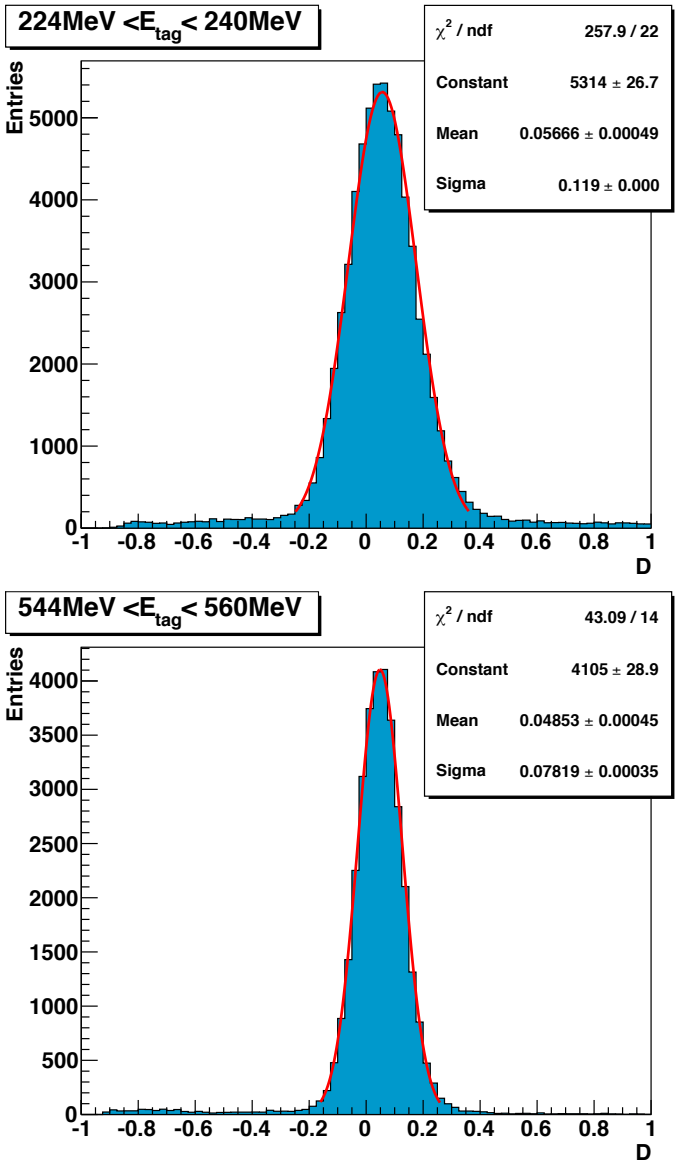

Figure 5.9: Two examples of energy bins with the Gaussian fit. Higher energy bins have smaller distribution width (σ), as expected.

For each bin a ratio was formed:

$$D = \frac{E_{cal} - C \cdot E_{tag}}{E_{tag}} \tag{5.3}$$

where E_{tag} is the tagged photon energy (as given by the energy tagger) and C is a constant coefficient. C represents the fraction of energy that is expected to be deposited in the module and simulations have shown that it's approximately 0.95; the remaining 5% escapes the volume of the module. The D distribution for every bin was fitted with a Gaussian function, as shown in Figure 5.9. The width of the Gaussian reflects the energy resolution for the specific region of the energy spectrum of the bin.

The general form of the energy resolution for a sampling calorimeter is given by:

$$\frac{\sigma_E}{E} = \frac{a}{\sqrt{E(GeV)}} \oplus b \oplus \frac{c}{E} \tag{5.4}$$

However, it has been shown that for Prototype 1 the noise term ($\frac{c}{E}$) was consistent with zero [21], therefore the fit function used was Equation 5.5.

$$\frac{\sigma_E}{E} = \frac{a}{\sqrt{E(GeV)}} \oplus b \tag{5.5}$$

The resolution plotted versus the mean tagger energy for the respective bin is shown in Figures 5.10, and 5.11, for all the different data sets.

The energy resolution at 90° is shown in Figure 5.10. It was used as a point of reference for the methodology used to extract the energy resolution. The floor term ($b = 1.7 \pm 0.3$) is sensitive to the parameters of the Gaussian fit. Small variations in the properties of the fit result in large variations in the floor term. Typically b is

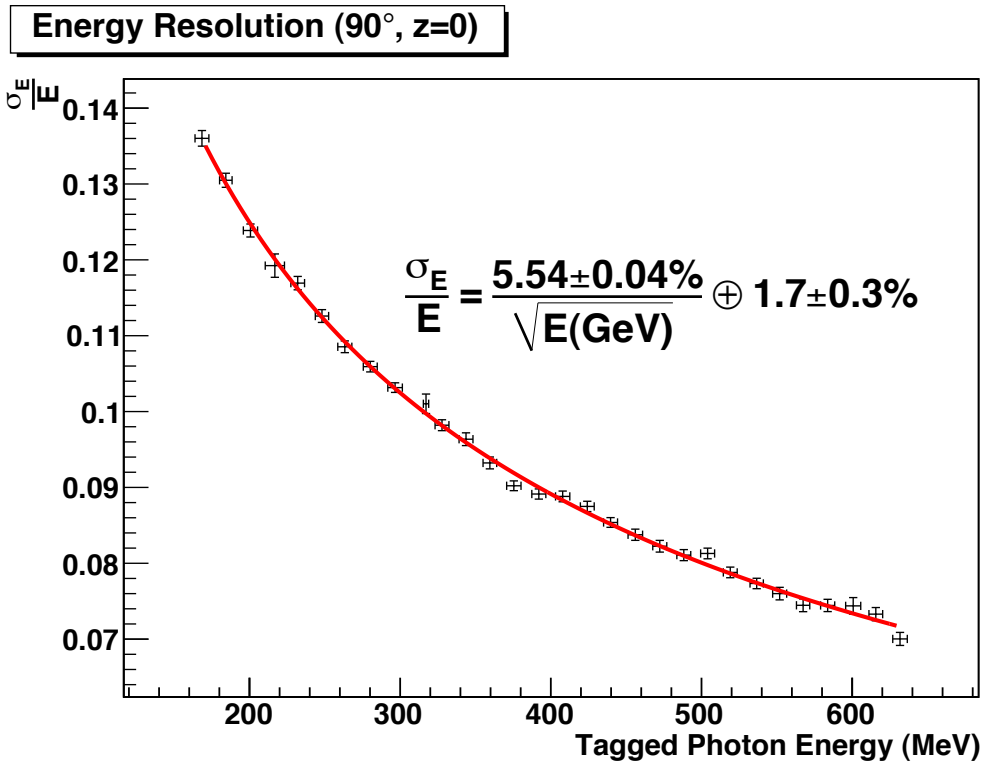

Figure 5.10: Energy resolution at 90° as a function of tagged photon energy.

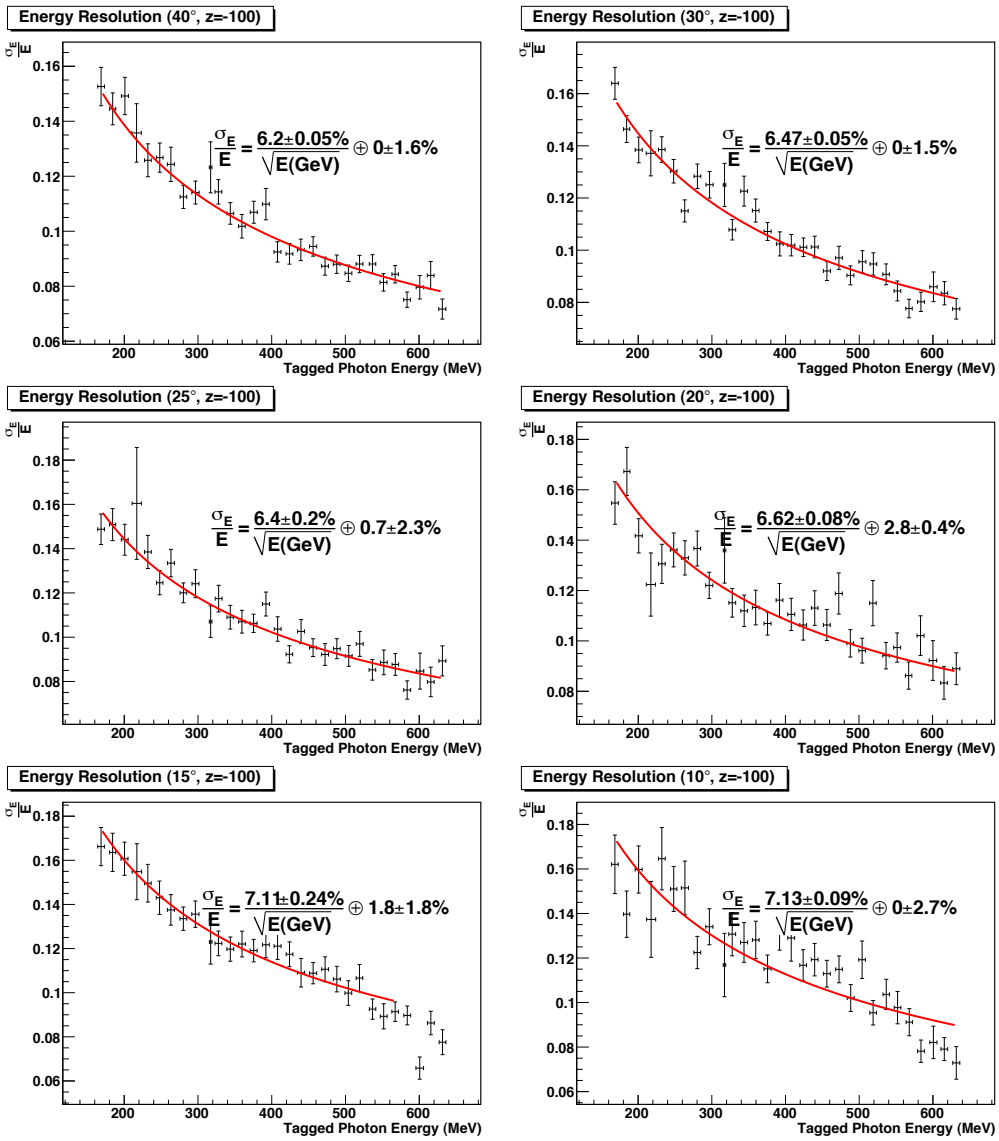

Figure 5.11: Energy resolution for various angles of incidence. As the angle decreases the energy term degrades. This is expected because the energy leakage from the sides and also from backsplash out of the front face of the module, increases. Discussion about the floor term is given in the text.

close or even less than 1% [30] and it's contribution to the energy resolution can be neglected especially in the quadratic form of Equation 5.5. To effectively pinpoint the floor term one would have to use energies up to 2 GeV, which were not available during beam test. On the other hand, the energy term ($a = 5.54 \pm 0.04$) is stable under fit parameter variations and in agreement with past calculations [21].

The energy resolution for angles other than 90° is shown in Figure 5.11 and was extracted using the same method. The uncertainties for these angles are larger primarily due to the lack of sufficient statistics (the number of events for the 90° runs is an order of magnitude larger). Individual points that have even larger uncertainties correspond to the bands that were excluded from the tagger spectrum, resulting in even lower statistics. Excluding those points from the resolution analysis did not show significant improvement and that is why they were not excluded from the analysis.

As the angle of incidence decreases, the fits to the data become less accurate since the width of the D distribution increases. At the very low angle of 10°, the energy leakage out of the front face of the module increases and that deteriorates the energy resolution. This is not alarming since the BCAL is not required to detect particles accurately below 10.5°. In that region of shallow angles ($\theta \leq 12°$), combined data from both the FCAL and the BCAL would be required and it is expected that many events will not be reconstructable although others have shown that the effects will be insignificant. For the reason explained above, the 10° data are shown in the resolution graphs (Figure 5.11) but were not used further in the analysis.

Parameters a and b in Equation 5.5 depend on the angle of incidence as shown in Figure 5.12. Parameter a, which represents fluctuations due to the stochastic nature of bremsstrahlung and pair production decreases as the angle of incident increases. This is expected since fluctuations from intrinsic properties of the interaction mech-

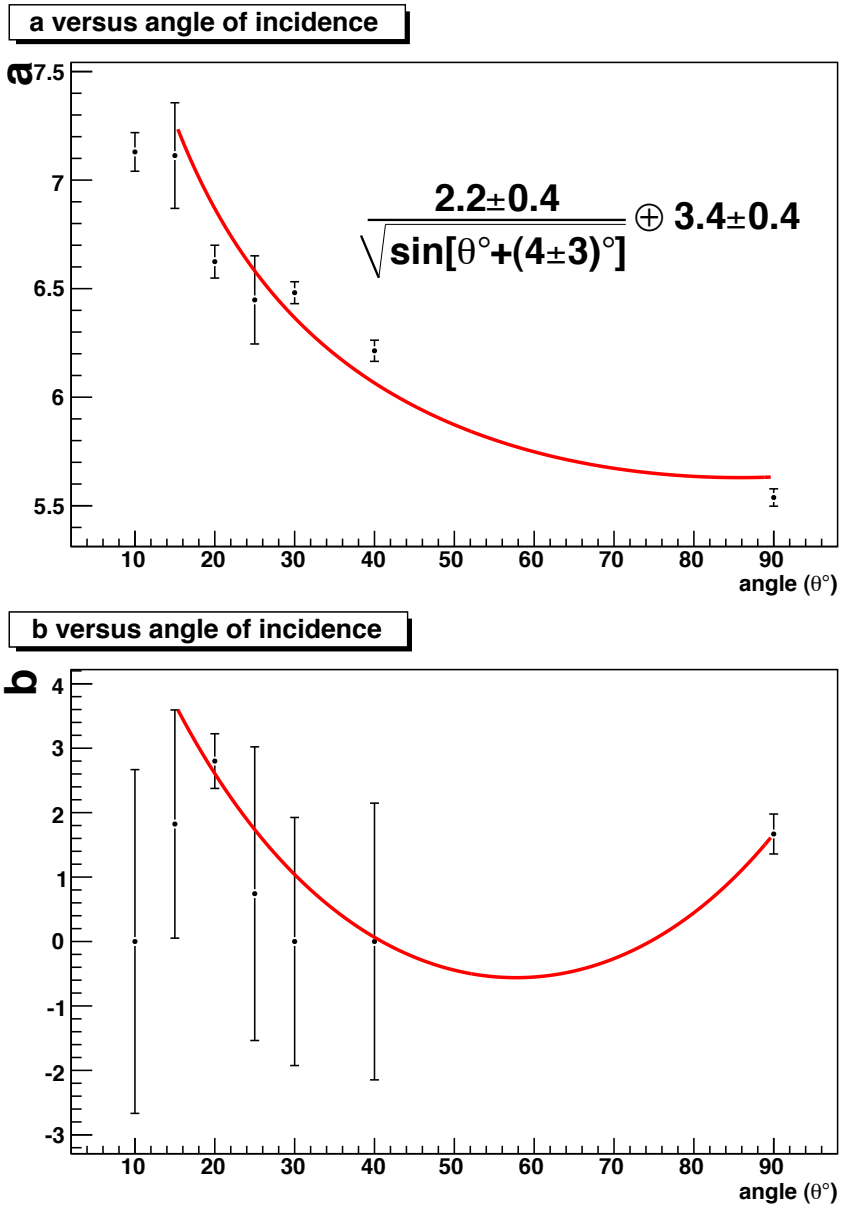

Figure 5.12: Resolution parameter a and b versus angle of incidence. a steadily decreases as the angle of incidence increases. The energy range was not wide enough to effectively determine parameter b, which is reflected by the large uncertainties. A fit was attempted but it does not represent the data accurately.

anisms increase with the number of particles created as the shower develops. As the angle decreases, the particles transverse more of the radiator mass resulting in more interactions and of course increased fluctuations [15].

Chapter 6

Conclusions

The GlueX experiment is expected to shed light in an as yet minimally explored area in the physics realm: the confinement region that holds together the fundamental building blocks of the world around us. Scientists from 15 universities around the world have been working together to put together a state of the art detector capable of detecting the properties of decaying particles that will lead GlueX to its desired goal.

The detector consists of several subsystems, each one constructed under strict requirements, in order to perform its task with high efficiency. The BCAL is one of the most important subsystems of the detector and is expected to determine the energy of neutral particles, as well as charged particles, travelling at azimuthal angles in the interval of $\sim 12^{\circ}$ to $\sim 125^{\circ}$. It is a barrel shaped, electromagnetic, sampling calorimeter, consisting of layers of thin lead interleaved with layers of scintillating fibres glued together with epoxy. It is of great importance that the BCAL detects decay products with good resolution, preferably over the entire energy spectrum in order for the subsequent analysis of data to yield the desired results. To that end, Monte Carlo simulations were carried out as part of the R&D phase for the BCAL

such as the ones presented in Chapter 4.

The Monte Carlo was designed to address the question of whether using thinner lead sheets to build the lead, scintillating fibre matrix would positively affect the performance of the BCAL. Simulations were carried out for a single module and in addition to the nominal geometry, which was tested once again, two new geometries were tested for the shape of the shower profile, resolution, fractional energy deposition and leakage:

- The *thin* geometry consisting of 0.2 mm thick lead sheets resulting in 1.11 mm radial pitch, significantly thinner than the 0.5 mm lead sheets of the *nominal* geometry with a radial pitch of 1.24 mm, yielded the expected results. A smooth shower profile was observed with the shower maximum occurring deeper in the detector than the nominal geometry, a result of the reduced density. Improved energy resolution was achieved when compared to the *nominal* geometry resolution, especially at 14° and 45°. The fractional energy deposition increased as expected by the relative increase of the scintillating fibre volume. Leakage was increased and that is reflected by the floor term of the resolution at 90°.

- The *hybrid* geometry, a mixture of the *nominal* and *thin* geometry, was simulated in an attempt to reduce the leakage out the back of the module relatively to the *thin* geometry and at the same time maintain its improved resolution.

The results from the Monte Carlo simulations were in good agreement with past simulations for the *nominal* geometry. The *thin* and *hybrid* geometries exhibited improved energy resolution and sampling fraction for the forward angles relative to the *nominal*. However, both *thin* and *hybrid* geometry showed increased leakage which degrades the energy resolution at incident angles close to perpendicular to the module. The *hybrid* geometry was able to handle the energy leakage better than

the *thin* geometry, but the non linearity introduced by the change in geometry will be a challenge to account for in the subsequent analysis. In addition, the specifications for the BCAL construction and anticipated operation set in 2008, rendered the completion of this geometrical study purely academic, mainly in the sense that the timetable of the BCAL did not allow for the R&D required to swage thinner lead. It was decided within GlueX to not pursue either the thin or the hybrid designs further. Moreover, since the initiation of this study it has been decided that the SiPMs are going to be cooled down, thus reducing the dark current and decreasing the effective energy thresholds. This is because improved signal-to-noise ratio allowed by the cooling can compensate for the weaker signals generated by low energy particles traversing the BCAL and therefore not requiring a change in the geometry of the calorimeter itself.

In Chapter 5 the energy resolution at 90° was extracted from beam test data once again for Prototype-1, and was found to be in agreement with past studies. A different dataset, at $z = -100\ cm$, instead of the centre of the volume ($z = 0\ cm$), was used to extract the energy resolution for different angles of the incident photons and the same method as for the 90° was used. The resolution was found to behave as expected: the energy dependent term a increases as the angle of incidence decreases as a consequence of the reduced number of fibre layers traversed by the shower (sampling frequency). The behaviour of the floor term was impossible to determine with sufficient accuracy due to the lack of data at higher energies. It is expected that the floor term increases at shallow angles below 40°, due to the increased leakage that occurs from the front of the module, a fact further supported by the simulations carried out in Chapter 4, which showed increased leakage at smaller angles.

Chapter 7

Suggestions for future work

The extraction of the timing resolution and the number of photoelectrons for the shallow angle dataset, which are very interesting, was not done due to time restrictions and is left as a future plan. It would be interesting to pursue this analysis due to the fact that the majority of the energetic particles are expected to enter the BCAL at shallow angles. Further Monte Carlo simulations where the attenuation length and the photon statistics have been taken into account would be beneficial as they would provide means to compare the results of the beam test data analysis.

Bibliography

[1] Donald H. Perkins. *Introduction to High Energy Physics*. Cambridge University Press, 2001.

[2] M. Gell-Mann. Schematic Model of Baryons and Mesons. *Phys. Lett.*, 8:214, 1964.

[3] A. Abele et al. A High Resolution Search for the Tensor Glueball Candidate $\xi(2230)$. *Phys. Lett.*, B520, 175, 2001.

[4] E. Aker et al. The crystal carrel detector at LEAR. *Nucl. Instr. Meth.*, A321:69, 1992.

[5] R. Gupta. Introduction to Lattice QCD. 1998.

[6] T. Barnes, F. E. Close. *Phys. Lett.*, B123:89, 1983.

[7] T. Barnes, F. E. Close. *Phys. Lett.*, B128:277, 1983.

[8] T. Barnes, F. E. Close, F. de Viron. *Nucl. Phys.*, B224:241, 1983.

[9] T. Barnes, editor. *The Bag Model and Hybrid Mesons*, SIN School of Strong Interactions, Zuoz Switzerland, 1985.

[10] T. Barnes, editor. *The Exotic Atoms of QCD: Glueballs, Hybrids and Baryonia*. School of Physics of Exotic Atoms, 1984.

[11] Nathan Isgur and Jack Paton. Flux-Tube Model for Hadrons in QCD. *Phys. Rev. D*, 31(11):2910–2929, Jun 1985.

[12] T. Barnes, editor. *Exotic Mesons, Theory and Experiment*, 2000.

[13] GlueX Collaboration. The Science Driving the 12 GeV Upgrade of CEBAF. Technical report, Jefferson Lab, 2001.

[14] GlueX Collaboration. The GlueX Experiment, A Search for QCD Exotics Using a Beam of Photons. Technical report, Jefferson Lab, 2004.

[15] R. Wigman. *Calorimetry.* Oxford Science Publications, 2000.

[16] M. Adinolfi et al. *Nucl. Instr. Meth.*, A494:326, 2002.

[17] M. Adinolfi et al. *Nucl. Instr. Meth.*, A482:364, 2002.

[18] M. Adinolfi et al. *Nucl. Instr. Meth.*, A461:344, 2001.

[19] C. Amsler et al. (Particle Data Group). Photon and Electron Interaction in Matter. Phys. Lett. B667:272–277, 2008 and 2009 (partial update for the 2010 edition).

[20] F. Cervelli. Pisa University, KLOE Collaboration, Private Communications. 2001.

[21] B.D. Leverington et al. Performance of the prototype module of the electromagnetic barrel calorimeter. *Nucl. Instr. Meth.*, A 596:327–337, 2008.

[22] Z. Papandreou. BCAL Calorimetry Response. Technical report, GlueX Collaboration, 2007. GlueX-doc-840-v2.

[23] R. Brun et al. GEANT: Simulation Program for Particle Physics Experiments, User Guide and Reference Manual. Technical report, 1978.

[24] B. Rossi. *High Energy Particles*. Prentice-Hall, Inc., Engelwood Cliffs, NJ, 1952.

[25] B. Leverington. Sampling Fraction Fluctuations. Technical report, GlueX Collaboration, 2007. GlueX-doc-827-v3.

[26] Z. Papandreou, B. Leverington, G.J. Lolos. Spectral response of scintillating fibers. *Nucl. Instr. Meth.*, 2008.

[27] A. Semenov, I. Semenova. First Article Fibers: Re-Analysis of JLab Data in Regina. Technical report, University Of Regina, 2009.

[28] A. Semenov. Report on test of first article fibers from Kuraray. Technical report, University Of Regina, 2009.

[29] J.T. O'Brien et al. The bremsstrahlung tagged photon beam in Hall-B at JLab. *Nucl. Instr. Meth.*, 440:263–284, 2000.

[30] C. Amsler et al. (Particle Data Group). Photon and Electron Interaction in Matter. Physics Letters B667:304, 2008 and 2009 (partial update for the 2010 edition).

Appendix A

Energy leakage at 45° and 14°

The energy leakage at 45° and 14° are shown in Figure A.1 and Figure A.2, respectively.

Energy leakage from the sides of the module is not added to the total energy leakage because it will be detected by adjacent modules. It is independent of the angle of incidence and increases as the density of the module in radiation lengths decreases, which is the expected behaviour.

Energy leakage from the ends of the module, where the readout devices will be mounted, is consistent with zero for all geometries and different angles of incidence of the incoming photons.

Leakage from the front of the module increases as the angle decreases and the density of the module decreases. It is possible that particles escaping one of the BCAL modules, from its inner surface, can be detected by other modules although their reconstruction would be complicated. Monte Carlo simulations of the entire detector are needed for a definitive answer and were not pursued in this work.

Energy leakage out the back, which is the most important since it directly affects the energy resolution and thus the performance of the calorimeter, decreases as the

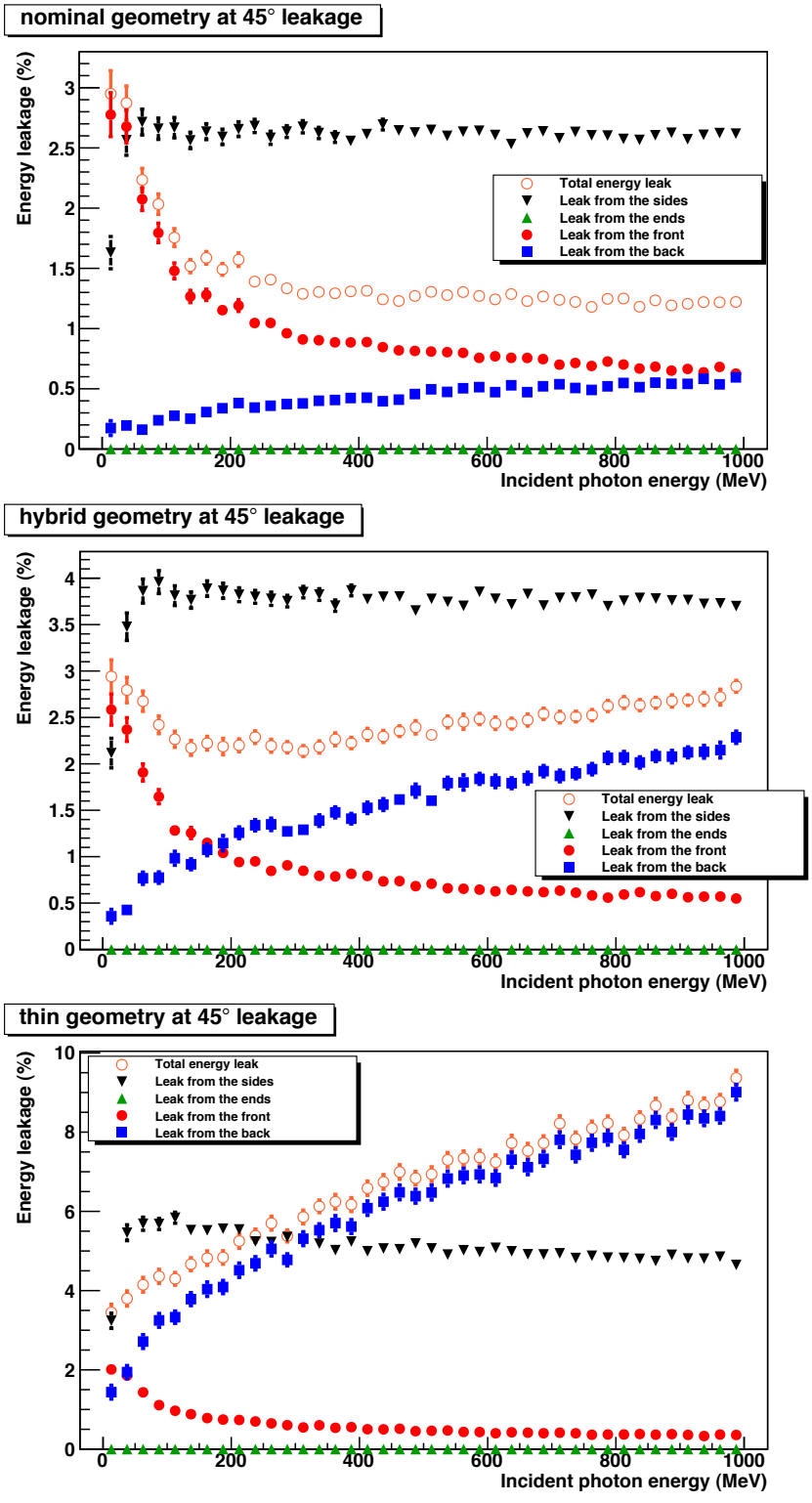

Figure A.1: Energy leakage at 45° angle of incidence.

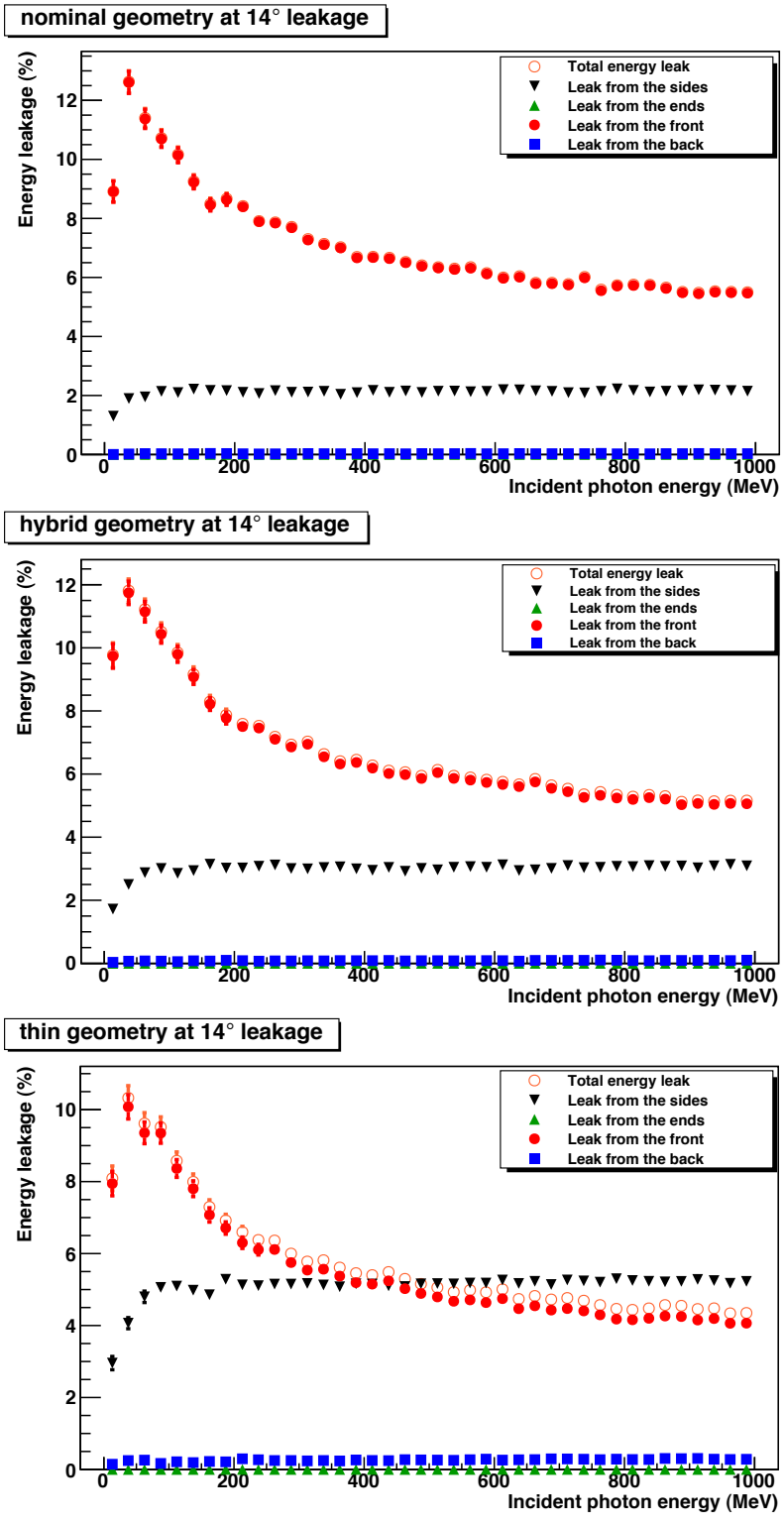

Figure A.2: Energy leakage at 14° angle of incidence.

angle decreases given the same geometry. It also decreases as the density of the module increases for a given angle. This is the expected behaviour.

Finally the total energy leakage is consistent with the fractional energy deposition, which affirms the reliability of the simulations.